

Deep Learning Improves Global Satellite Observations of Ocean Eddy Dynamics

Scott A. Martin¹, Georgy E. Manucharyan¹, and Patrice Klein^{2,3}

¹School of Oceanography, University of Washington, Seattle, WA, USA

²Jet Propulsion Laboratory, California Institute of Technology, Pasadena, CA, USA

³Laboratoire de Météorologie Dynamique, École Normale Supérieure, Paris, France

Key Points:

- We develop the first deep learning global estimates of surface ocean currents from multi-modal satellite observations.
- Our deep learning method is able to map surface currents with state-of-the-art resolution and accuracy.
- The diagnosed kinetic energy cascade is an order of magnitude higher compared to conventional altimetry products.

Corresponding author: Scott A. Martin, smart1n@uw.edu

14 Abstract

15 Ocean eddies affect large-scale circulation and transfer energy between scales through
 16 non-linear eddy interactions. This eddy-induced kinetic cascade depends on the strain
 17 rate, which is strongly sensitive to the precise geometry and configuration of eddies. How-
 18 ever, surface currents estimated globally from altimetry smooth and distort eddies, severely
 19 underestimating the strength of non-linear eddy interactions and the resulting cascade.
 20 Here, we present the first global deep learning estimate of surface currents from multi-
 21 modal satellite observations of sea surface height and temperature. We achieve a 30%
 22 improvement in spatial resolution over the community-standard sea surface height prod-
 23 uct and demonstrate that it significantly improves our observations of eddy dynamics.
 24 In many regions, this improved resolution leads to nearly an order-of-magnitude increase
 25 in the upscale kinetic energy cascade, emphasizing its crucial role in the seasonality of
 26 large mesoscale eddies. Our study suggests that deep learning can be a powerful paradigm
 27 for satellite oceanography.

28 Plain Language Summary

29 We developed a deep learning method to estimate global maps of surface ocean cur-
 30 rents from satellite observations with significantly improved resolution and accuracy com-
 31 pared to existing methods. These maps dramatically improve our ability to observe eddy
 32 dynamics and the impact of eddies on the transfer of energy between scales in the ocean.
 33 Our study suggests that deep learning can be a powerful paradigm for satellite oceanog-
 34 raphy.

35 1 Introduction

36 Mesoscale eddies (50-300 km) are a critical component of the global ocean circu-
 37 lation, transporting dynamical and biogeochemical tracers (Wunsch, 1999; Jayne & Marotzke,
 38 2002; Zhang et al., 2014). Despite being the ocean’s dominant reservoir of kinetic en-
 39 ergy (KE), the sources and sinks of mesoscale eddy KE remain poorly constrained (Ferrari
 40 & Wunsch, 2009). One major process affecting mesoscale KE is the transfer of KE be-
 41 tween scales by non-linear eddy interactions, known as the KE cascade (Scott & Wang,
 42 2005; Aluie et al., 2018; Klein et al., 2019). There is growing evidence that these non-
 43 linear eddy interactions induce a strongly seasonal upscale KE cascade, KE transfer from
 44 small to large scales, that is intensified in winter and spring (Sasaki et al., 2014; Qiu et
 45 al., 2014; Uchida et al., 2017; Schubert et al., 2020; Ajayi et al., 2021; Balwada et al.,
 46 2022; Garabato et al., 2022; Steinberg et al., 2022; Lawrence & Callies, 2022; Schubert
 47 et al., 2023; Storer et al., 2023). The strength of non-linear eddy interactions and the
 48 KE cascade are set by the vorticity and strain of eddies (Aluie et al., 2018; Klein et al.,
 49 2019), which are highly sensitive to the precise geometry of eddies. There is thus a need
 50 for global observations of eddies with sufficient resolution to accurately diagnose vortic-
 51 ity and strain - this motivates our study.

52 Satellite observations of the surface expressions of eddies are a powerful observing
 53 system for eddy dynamics since satellites resolve a wide range of scales compared to in
 54 situ observations (Klein et al., 2019), however, there are challenges in inferring surface
 55 currents from satellite observables. Satellite altimetry allows the estimation of eddies by
 56 mapping their expression in sea surface height (SSH), which is used to estimate surface
 57 geostrophic currents (Chelton et al., 2001). Conventional altimeters measure SSH and
 58 resolve mesoscale eddies along each satellite’s track (Dufau et al., 2016) but leave large
 59 gaps between tracks that must be interpolated to diagnose eddy dynamics. Meanwhile,
 60 satellites observe high-resolution 2D snapshots of SST but there are gaps due to clouds
 61 and the relationship between SST and surface currents is complex (Isern-Fontanet et al.,
 62 2006, 2014; Rio et al., 2016).

63 Conventionally, surface currents are estimated either via data assimilation (DA)
64 (Jean-Michel et al., 2021; Le Guillou et al., 2021, 2023) or objective analysis (OA) of SSH
65 (Taburet et al., 2019; Ubelmann et al., 2015, 2021, 2022). DA provides 3D state estimates
66 consistent with the physics of a numerical model, typically a general circulation model
67 (GCM), but that suffer high errors in SSH and surface currents (Jean-Michel et al., 2021)
68 due to GCM biases and the lack of high-resolution 3D in-situ observations. In contrast,
69 OA allows to estimate only the 2D SSH field (Taburet et al., 2019; Ubelmann et al., 2015,
70 2021, 2022), from which currents can be estimated through geostrophy and further em-
71 pirical corrections for winds (Rio et al., 2014), equatorial dynamics (Lagerloef et al., 1999),
72 and cyclo-geostrophy (Penven et al., 2014; Cao et al., 2023), or potentially using machine
73 learning (Sinha & Abernathey, 2021; Xiao et al., 2023). Surface currents derived from
74 OA SSH fields are uncontaminated by biases due to unresolved physics in GCMs and
75 have more accurate eddies than DA. However, linear covariance models employed in OA
76 smooth and distort eddies (Ballarotta et al., 2019), leading to a significant under-estimation
77 of crucial dynamical quantities, like vorticity and strain. There is thus a trade-off be-
78 tween the accuracy and physical realism of eddies with DA and OA.

79 In recent years, deep learning has emerged as an alternative approach for estimat-
80 ing surface currents. A number of proof-of-concept studies demonstrate that neural net-
81 works can be trained to map SSH or surface currents from altimeter observations through
82 either ‘simulation learning’ using synthetic data from GCMs (Fablet et al., 2021; Manucharyan
83 et al., 2021; Buongiorno Nardelli et al., 2022; Beauchamp et al., 2022; Fablet et al., 2023;
84 Thiria et al., 2023; Febvre et al., 2023; Archambault et al., 2024; Kugusheva et al., 2024)
85 or ‘observation-only learning’ from real-world satellites (Martin et al., 2023; Archambault
86 et al., 2023). Deep learning allows the optimal mapping to emerge objectively from the
87 data by removing OA’s need to prescribe linear covariance models (Taburet et al., 2019;
88 Ballarotta et al., 2019), and also allows the use of SST observations as an additional in-
89 put to improve the mapping between altimeter observations (Buongiorno Nardelli et al.,
90 2022; Fablet et al., 2023; Martin et al., 2023; Archambault et al., 2023, 2024). Simula-
91 tion learning showed promising results on synthetic observations in idealized proof-of-
92 concept studies. However, transferring these methods to real-world observations remains
93 a challenge since GCMs are not exact analogs of the real-world ocean and neural net-
94 works can behave unpredictably when applied to data different from that used during
95 training. This domain gap can be partly addressed through fine-tuning on real-world ob-
96 servations (Febvre et al., 2023; Archambault et al., 2024). More fundamentally, simu-
97 lation learning blurs the boundaries between observations and GCMs, analogous to DA.
98 In contrast to simulation learning, observation-only learning is uncontaminated with GCM
99 biases and can provide an observational product with higher resolution than OA, as was
100 demonstrated by regional proof-of-concept studies (Martin et al., 2023; Archambault et
101 al., 2023).

102 Extending regional proof-of-concept studies to global SSH mapping poses a signif-
103 icant challenge for deep learning because the Global Ocean exhibits spatiotemporally di-
104 verse dynamics. Given the sparsity of the altimetry record for observation-only learn-
105 ing, it remains to be demonstrated that a neural network can generalize across all dy-
106 namical regimes. We hypothesize that if observation-only learning manages to create global
107 SSH maps with enhanced resolution, they will radically improve global observations of
108 non-linear eddy dynamics. Here, we develop the first global deep learning estimates of
109 surface currents, evaluating their accuracy and ability to resolve non-linear eddy dynam-
110 ics and their resulting KE cascade. By disseminating our new global SSH product, we
111 hope to enable more accurate studies of eddy dynamics and their impact on general ocean
112 circulation, marine ecosystems, and climate.

113 2 Methods

114 2.1 NeurOST: Global SSH Maps from Altimetry and SST Using Deep 115 Learning

116 We train a neural network to map SSH from sparse altimeter observations (E.U.
117 Copernicus Marine Service Information (CMEMS), 2024b, 2024a) and gridded SST (JPL
118 MUR MEaSURES Project, 2015). Our approach, illustrated in Figure 1, builds upon that
119 described in our recent proof-of-concept study (Martin et al., 2023) and is described in
120 full in S.I. S1.1-5.

121 We use ‘self-supervised’ learning, taking a time series of altimeter observations within
122 a local subdomain (30 days by 960 km by 960 km) from all but one of the available alt-
123 timeters alongside the corresponding SST as input to a neural network tasked with re-
124 constructing 2D SSH. The objective minimized during training is the mean square er-
125 ror of the mapped SSH calculated against the withheld altimeter. We restrict the map-
126 ping to local subdomains since eddy dynamics are local, so a global ‘field of view’ is likely
127 unnecessary to reconstruct eddies in any local subdomain.

128 We use kernel-weighted averaging to combine thousands of overlapping subdomain
129 SSH maps together into a single global SSH map (S.I. S1.5 and Callahan et al. (2019)).
130 Using a large set of subdomain examples drawn from across the globe, we train a sin-
131 gle network to map SSH in all regions, achieving generalization across diverse regional
132 dynamics. By training a single global network rather than an ensemble of bespoke re-
133 gional networks we avoid arbitrarily dividing the globe into regions and learn a general
134 and robust SSH mapping. The network was trained on observations from 2010 to 2023,
135 with 2019 withheld for validation.

136 We refer to our method as ‘NeurOST (SSH-SST)’ (Neural Ocean Surface Topog-
137 raphy). To assess the value of SST we also trained a network to map SSH from altime-
138 try alone; ‘NeurOST (SSH)’.

139 2.2 Estimating Surface Currents from SSH

140 Large-scale ocean currents satisfy geostrophic balance, allowing surface currents
141 to be estimated from SSH through geostrophy (S.I. Equation 1). The limitations of geostro-
142 phy and potential empirical ageostrophic corrections (Lagerloef et al., 1999; Rio et al.,
143 2014; Penven et al., 2014; Cao et al., 2023) are discussed in S.I. S1.1 where we also show
144 diagnostics of eddy dynamics (e.g. KE cascade) are only weakly sensitive to the correc-
145 tion for cyclo-geostrophy of Penven et al. (2014). Thus throughout this manuscript the
146 presented surface currents were calculated using geostrophy.

147 2.3 SSH Mapping Evaluation: Observing System Experiment (OSE)

148 We employ an observing system experiment (OSE) to evaluate the SSH maps. Com-
149 parisons to existing methods are achieved using an Ocean Data Challenge (Metref et al.,
150 2023; Metref & Ballarotta, 2023) in which developers of different methods implement them
151 on a common experiment. In the OSE used here we create global SSH maps for 2019 us-
152 ing all altimeters apart from Saral/Altika which is used to evaluate the maps. Accuracy
153 is evaluated using root mean square error (RMSE) and we quantify the maps’ effective
154 spatial resolution following Ballarotta et al. (2019) to estimate the smallest resolved wave-
155 length. We compare NeurOST to the community-standard ‘DUACS’ product (Le Traon
156 et al., 1998; Taburet et al., 2019) as well as to the ‘MIOST’ method (Ubelmann et al.,
157 2021; Ballarotta et al., 2023). Surface geostrophic currents are evaluated using drifters
158 (E.U. Copernicus Marine Service Information (CMEMS), 2024c). Additionally, we com-
159 pare NeurOST to proof-of-concept methods in the Gulf Stream Extension using a sim-

160 ilar Ocean Data Challenge that was regional in scope (Ballarotta et al., 2021). More de-
 161 tails are in S.I. S1.6-7.

162 **2.4 Eddy Dynamics Evaluation: Observing System Simulation Exper-** 163 **iment (OSSE)**

164 While the OSE evaluates SSH maps, we cannot use it to evaluate eddy dynamics
 165 (vorticity and strain) inferred from SSH as this requires access to the full 2D eddy field.
 166 We therefore conduct an observing system simulation experiment (OSSE) where we gener-
 167 ate synthetic altimeter observations from the 1/12° GLORYS reanalysis (Jean-Michel
 168 et al., 2021; E.U. Copernicus Marine Service Information (CMEMS), 2024d) and use them
 169 in combination with GLORYS SST as input to NeurOST with no additional training on
 170 GLORYS. We then compare the resulting NeurOST maps to the 2D ground-truth from
 171 GLORYS to evaluate eddy dynamics diagnostics, specifically surface geostrophic currents
 172 and vorticity for which we define normalized skill scores representing the fraction of vari-
 173 ance explained (S.I. S1.11). This point-wise comparison to GLORYS cannot be made
 174 for DUACS since this method is not open source, preventing its implementation on sim-
 175 ulated observations. GLORYS is a flawed representation of real-world eddy dynamics
 176 due to its coarse grid resolution. Nonetheless at larger scales it provides a physically plau-
 177 sible inter-relation between SSH, SST, and surface vorticity which we use to assess the
 178 reliability of NeurOST eddy dynamics.

179 **2.5 Kinetic Energy Cascade Diagnosis**

180 We use NeurOST surface geostrophic currents to diagnose the strength of the KE
 181 cascade in a range of regions through coarse-graining (Aluie et al., 2018; Storer et al.,
 182 2022; Storer & Aluie, 2023; Storer et al., 2023). The strength of the KE cascade is given
 183 by the spectral KE flux, which quantifies KE transfer from larger to smaller scales at each
 184 wavelength. A positive flux indicates a downscale (forward) cascade, whereas a negative
 185 value indicates an upscale (inverse) cascade. More details are in S.I. S1.12.

186 **3 Results**

187 **3.1 State-of-the-Art Global SSH Maps Using Deep Learning**

188 Our new global SSH maps (NeurOST SSH-SST) show rich dynamical structures
 189 associated with western boundary currents, abundant mesoscale eddies in the extratrop-
 190 ics, and large-scale equatorial waves in the tropics (Figure 1).

191 The effective resolution of our maps is improved compared to DUACS throughout
 192 the Global Ocean, with a pronounced improvement in western boundary currents and
 193 the subtropics where we resolve wavelengths 30% smaller (Figure 2b,d and Table S1).
 194 The global RMSE of the mapped SSH is 6% lower than DUACS, while reductions in the
 195 RMSE of small mesoscale signals (70-250km wavelengths) reach 20% in regions of intense
 196 eddy activity (Figure 2a,c,e and Table S1). Similarly, NeurOST outperforms MIOST in
 197 almost all regions, especially for small mesoscale signals, making our method state-of-
 198 the-art in global SSH mapping (Figure S1 and Table S1).

199 Using SST improves the mapping of SSH throughout the Global Ocean (Figure 2f
 200 and Table S1). To assess the utility of SST, we compare the performance of NeurOST
 201 with and without SST. The mapping of small mesoscales is improved using SST, espe-
 202 cially in the extratropics where mesoscale SSH and SST are correlated (Cornillon et al.,
 203 2019) (Figure 2f and Table S1). SST is especially impactful when few altimeters are avail-
 204 able (Table S3). While observations from six satellite altimeters were used to create the
 205 maps compared above, for much of the altimetry era there were only two altimeters oper-
 206 ational, causing eddies in DUACS to be severely smoothed. We evaluated our network

207 using only two altimeters as input and found that in most regions NeurOST SSH-SST
 208 with just two altimeters yields higher-resolution SSH than DUACS achieves with six (Ta-
 209 ble S3). This highlights the power of using deep learning and SST to extract maximum
 210 value from the now thirty-year altimetry record.

211 NeurOST maps SSH across all regions, unlike prior studies which trained bespoke
 212 region-specific networks. While regional networks (Martin et al., 2023; Febvre et al., 2023)
 213 in the Gulf Stream offer marginally improved SSH mapping compared to our global net-
 214 work (Ballarotta et al., 2021) (Table S2), fine-tuning on a smaller set of observations from
 215 the Gulf Stream Extension (S.I. S1.6) brings NeurOST in line with state-of-the-art re-
 216 gional networks (Table S2). This shows the potential for further refinement of NeurOST
 217 by end users interested only in a single region.

218 Surface geostrophic currents from our maps are more accurate when evaluated with
 219 drifter observations. NeurOST reduces the RMSE of surface currents significantly across
 220 the Global Ocean, especially in the subtropics where RMSE is reduced by 20% compared
 221 to DUACS (Figure S2). Discrepancies between the mapped currents and drifter obser-
 222 vations are due to both the accuracy of the mapped geostrophic current and the degree
 223 to which real-world currents are in geostrophic balance. Nonetheless, this large reduc-
 224 tion in RMSE demonstrates the significant improvement in the mapped currents and sur-
 225 face geostrophic currents from NeurOST have lower RMSE than surface currents from
 226 GLORYS (Jean-Michel et al., 2021) (Figure S3).

227 **3.2 Improved Physical Realism of Mesoscale Eddies**

228 Calculating vorticity and strain from the surface current maps appears to show a
 229 significant qualitative improvement in the realism of eddy dynamics in NeurOST (Fig-
 230 ure 3b,c,d and Movie S1). NeurOST vorticity shows an abundance of small mesoscale
 231 eddies with clearly defined boundaries between eddies, many of which are completely ab-
 232 sent in DUACS (Figure 3b,c). A contrasting view of eddy dynamics emerges when compar-
 233 ing the temporal eddy evolution: eddies appear to uniformly propagate westward in
 234 DUACS, while NeurOST eddies exhibit strong non-linear eddy interactions that deform
 235 each other’s vorticity cores, causing filamentation (Supplementary Movie S1). These better-
 236 resolved non-linear eddy interactions also manifest in the higher strain rate between ed-
 237 dies seen in NeurOST, evidenced by regions of highly positive Okubo-Weiss quantity (Fig-
 238 ure 3d, S.I. S1.10). This increased strain has important implications for eddy dynam-
 239 ics since it is associated with enhanced frontogenesis (Hoskins, 1982; Siegelman et al.,
 240 2020) and a stronger KE cascade (Aluie et al., 2018). While vorticity and strain appear
 241 qualitatively more realistic in NeurOST than in DUACS, their accuracy cannot be quan-
 242 tified using along-track SSH observations. To demonstrate that NeurOST does not in-
 243 troduce artificial eddies, we test its ability to reconstruct vorticity using synthetic ob-
 244 servations from a GCM with our OSSE framework (Section 2.4).

245 NeurOST, trained on real-world observations and applied now to synthetic obser-
 246 vations from GLORYS, skillfully reconstructs surface currents, especially in the subtrop-
 247 ics and western boundary currents, where it explains over 70% of the variance (Figure
 248 4a). Its skill deteriorates somewhat in regions of low variability, at high latitudes, and
 249 near coasts, where the observational training data is likely to significantly differ from the
 250 GLORYS simulation. Since vorticity is highly sensitive to small-scale SSH features, its
 251 overall reconstruction skill is slightly lower than that for surface currents. Nonetheless,
 252 NeurOST reconstructs a remarkable 50-80% of vorticity variance throughout the sub-
 253 tropics and western boundary currents. Comparing spatial patterns of vorticity and strain,
 254 it is clear that NeurOST misses smaller-scale filaments but skillfully reconstructs larger
 255 eddies and some larger filaments and is not prone to creating artificial eddies (Fig 4c-
 256 f). NeurOST reconstructs features as small as 50 km in some cases (see filaments in Fig-
 257 ure 4c-f). Thus, NeurOST can reasonably well reconstruct the 2D vorticity and strain

258 fields despite being trained only on real-world along-track SSH observations and never
 259 using real or simulated vorticity/strain fields during training. This remarkable general-
 260 izzability increases confidence in the smaller-scale dynamical features that appear in the
 261 NeurOST reconstruction of real-world observations. We thus proceed to highlight how
 262 these newly resolved features impact our understanding of eddy scale interactions.

263 3.3 Seasonal Kinetic Energy Cascade

264 A distinct seasonality in eddy dynamics emerges in our maps that was largely ab-
 265 sent in DUACS, with smaller scale eddies peaking in intensity in the winter and spring.
 266 The mesoscale KE and strain rate throughout the subtropics are 50-100% higher in Neu-
 267 rOST than in DUACS in winter/spring, whereas they are comparable in summer/autumn
 268 (Figure S4 & S5). We further explore this newly-resolved seasonality by focusing on the
 269 Subtropical North Pacific (SNP), which was the subject of prior studies of eddy season-
 270 ality (Qiu et al., 2014).

271 Eddy dynamics from NeurOST are strongly seasonal in the SNP, with enstrophy
 272 (the variance of vorticity) peaking in winter/spring implying intensified small-scale ed-
 273 dies (Figure 5a). This is corroborated by the KE wavenumber spectrum (S.I. S1.13) which
 274 has a shallower slope ($\approx k^{-2}$) in winter and spring than in summer and autumn ($\approx k^{-3}$)
 275 (Figure 5b), meaning energy is more concentrated at small scales in winter and spring.
 276 Notably, the peak in KE for small-scales ($<125\text{km}$) leads that for larger scales by two
 277 months (Figure 5c). It has been hypothesized that the delayed large-scale KE peak may
 278 partly be driven by an upscale KE cascade from submesoscales, which are most energetic
 279 during winter (Sasaki et al., 2014; Qiu et al., 2014). However, this hypothesis has not
 280 been confirmed using observations since low-resolution products like DUACS fail to re-
 281 solve the small-scale eddies that proliferate in winter/spring (Figure 5a,c), and hence un-
 282 derestimate the KE cascade (Arbic et al., 2013).

283 The KE cascade from NeurOST is upscale throughout the mesoscale range in the
 284 SNP, is strongly seasonal with a peak in the Spring, and is dramatically stronger than
 285 in DUACS (Figure 5d). Although some KE sources and sinks cannot be derived from
 286 surface currents (S.I. S1.12), the magnitude of the cascade appears more than sufficient
 287 to drive the increase in large-scale KE observed over winter/spring (Figure 5e). In con-
 288 trast, the overly-smooth DUACS product significantly underestimates the springtime KE
 289 cascade, obscuring the seasonality of the cascade and its role in driving the large-scale
 290 peak (Figure 5e). The role of the cascade in driving large-scale seasonality appears to
 291 be replicated in other subtropical regions, however this picture is less clear near west-
 292 ern boundary currents due to strong mesoscale variability associated with unstable west-
 293 ern boundary currents (Figure S6).

294 4 Discussion

295 Alongside this manuscript, we publish a NeurOST SSH product to facilitate future
 296 studies of eddy dynamics and the impacts of eddies on climate and marine ecosystems.
 297 Our high-resolution SSH maps generated using deep learning represent a large stride for-
 298 ward for the global observation of ocean eddy dynamics, providing state-of-the-art global
 299 surface currents. NeurOST allows to diagnose eddy dynamics with far greater physical
 300 realism than from existing altimetry products, revealing the crucial role of non-linear eddy
 301 dynamics and their associated KE cascade in driving the seasonality of mesoscale eddies.

302 Despite the improved resolution of NeurOST it does not yet resolve submesoscale
 303 eddies, smoothing scales below $O(100\text{km})$ (Table S4). Hence, the strength of the upscale
 304 cascade is likely still underestimated (Figure S7), and the potential presence of the down-
 305 scale cascade at submesoscales cannot be quantified. The recently launched Surface Wa-
 306 ter and Ocean Topography (SWOT) satellite, the first wide-swath altimeter (Morrow et

307 al., 2019; Fu et al., 2024), provides unprecedented 2D submesoscale-resolving SSH snap-
308 shots that could help characterize the KE cascade in the submesoscale range (Klein et
309 al., 2019; Carli et al., 2023). However, SWOT observations present new challenges for
310 inferring currents from SSH in the presence of unbalanced submesoscale SSH variabil-
311 ity and the mismatch between the fast-evolving submesoscale dynamics and SWOT’s long
312 orbital return times (Gaultier et al., 2016; Torres et al., 2018). Deep learning methods
313 to address these issues are under development and show promising results (Febvre et al.,
314 2022; Wang et al., 2022; Gao et al., 2024). As satellite oceanography enters a new submesoscale-
315 resolving era (Morrow et al., 2019; Fu et al., 2024), further development of deep learn-
316 ing methods will be crucial to best monitor surface currents and other essential climate
317 variables, like SST (Goh et al., 2023; Agabin et al., 2023).

318 5 Open Research

319 NeurOST maps generated using all available nadir altimeters and SST are avail-
320 able through NASA PO.DAAC (DOI in prep.). The 2019 NeurOST validation maps are
321 available here: <https://doi.org/10.7910/DVN/H4HQGD>. MUR SST data is available on
322 NASA PO.DAAC and the altimeter and surface drifter observations are available on CMEMS.
323 Ocean Data Challenges for global SSH mapping ([https://github.com/ocean-data-challenges/
324 2023a_SSH_mapping_OSE](https://github.com/ocean-data-challenges/2023a_SSH_mapping_OSE)) and for the Gulf Stream Extension ([https://github.com/ocean-
326 -data-challenges/2021a_SSH_mapping_OSE](https://github.com/ocean-
325 -data-challenges/2021a_SSH_mapping_OSE)) are on GitHub. Gulf Stream SSH maps
327 for Febvre et al. (2023) and Archambault et al. (2023) are at [https://doi.org/10.5281/
zenodo.8064113](https://doi.org/10.5281/
zenodo.8064113) and <https://gitlab.lip6.fr/archambault/visapp2023> respectively.

328 NeurOST code is available here: https://github.com/smartin98/Global_DL_SSH.
329 Coarse-graining code, FlowSieve (Storer & Aluie, 2023), is available here: [https://github
.com/husseinaluie/FlowSieve](https://github
330 .com/husseinaluie/FlowSieve).

331 Acknowledgments

332 The research was funded by NASA Grant 80NSSC21K1187. P.K. acknowledges support
333 from the SWOT Science Team and the QuikSCAT mission. The authors thank the cre-
334 ators of the Ocean Data Challenges, especially Sammy Metref and Maxime Ballarotta.
335 We acknowledge helpful discussions with Steven Brunton, Jinbo Wang, Brian Arbic, Quentin
336 Febvre, Tom Farrar, J. Xavier Prochaska, Peter Cornillon, and Christian Buckingham.
337 Computational resources supporting this work were provided by the NASA High-End
338 Computing (HEC) Program through the NASA Advanced Supercomputing (NAS) Di-
339 vision at Ames Research Center.

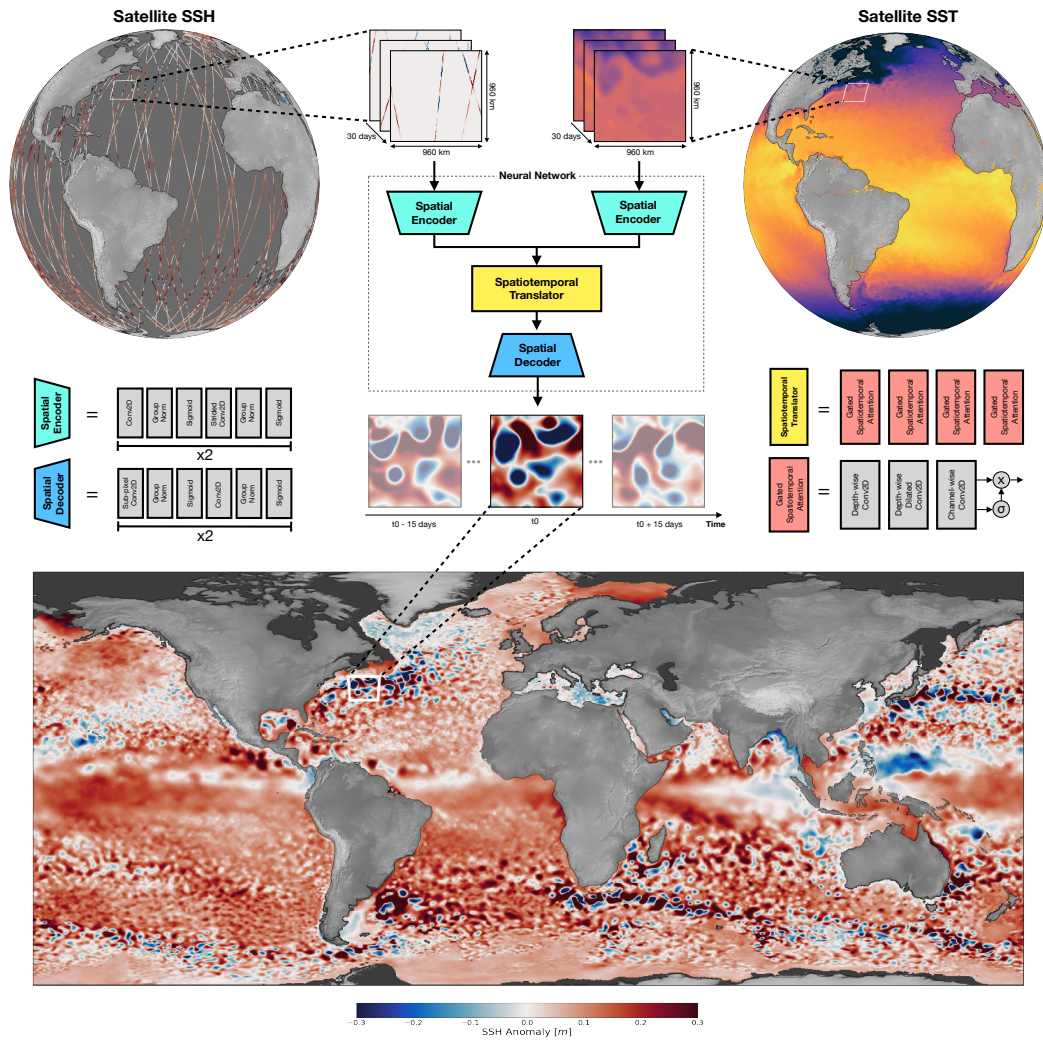


Figure 1. Schematic of NeurOST SSH-SST method for mapping SSH from satellite altimetry and SST.

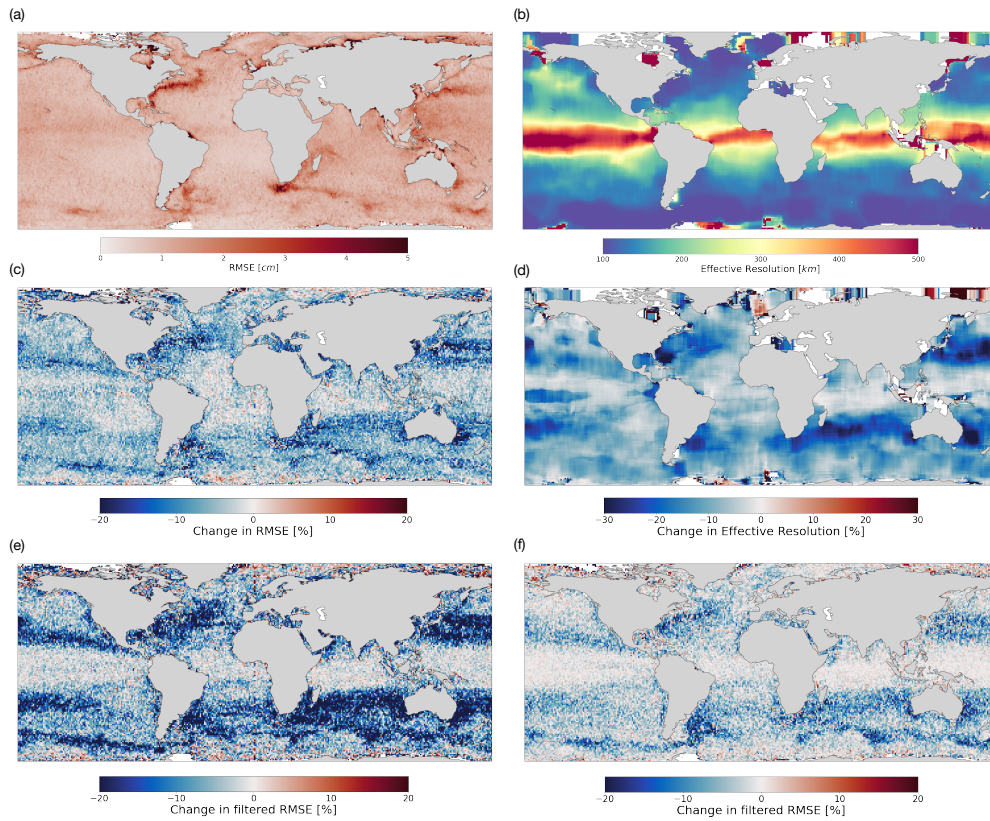


Figure 2. (a) RMSE of NeurOST SSH-SST compared to withheld altimeter. (b) Smallest resolved wavelengths (effective resolution) of NeurOST SSH-SST. (c) Change in RMSE of NeurOST SSH-SST compared to DUACS. (d) Change in effective resolution of NeurOST SSH-SST compared to DUACS. (e) Change in RMSE of small-scale (70-250km) signals of NeurOST SSH-SST compared to DUACS. (f) Change in RMSE of small-scale signals of NeurOST SSH-SST compared to NeurOST SSH.

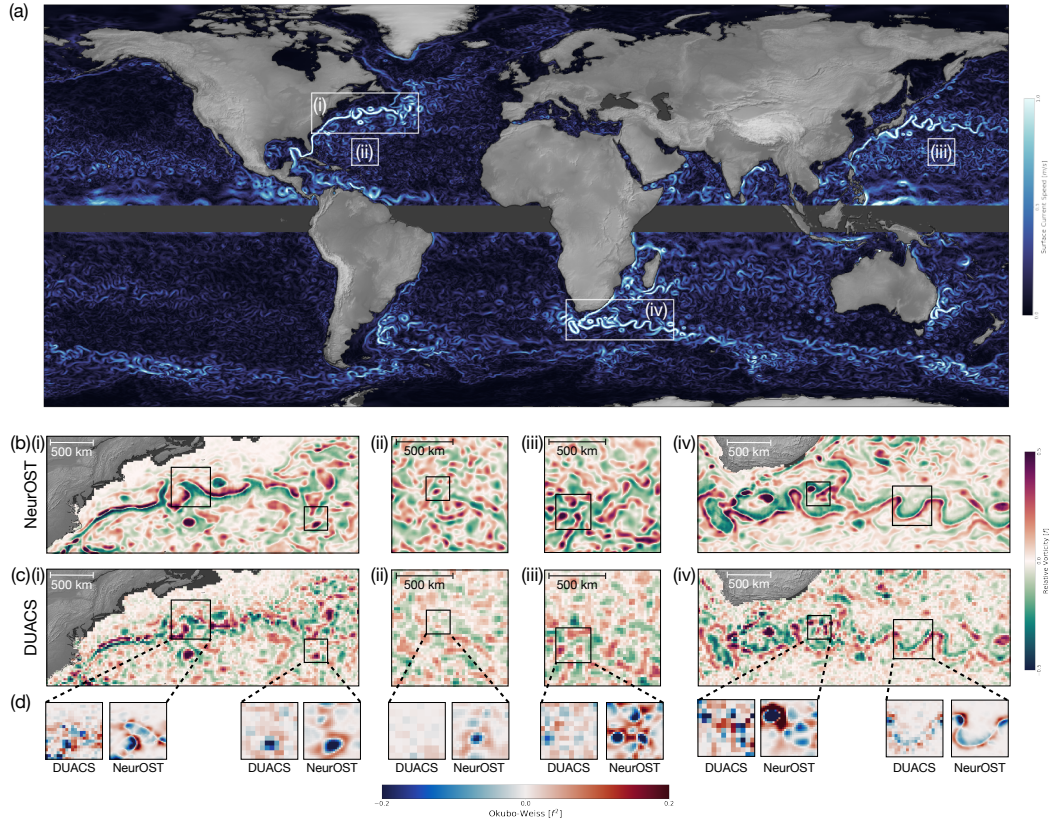


Figure 3. (a) Surface geostrophic current speed on March 1st 2019 derived from SSH maps made using NeurOST SSH-SST. (b) Relative vorticity from NeurOST SSH-SST. (c) Relative vorticity from DUACS. (d) Zoomed insets of Okubo-Weiss quantity for DUACS and NeurOST SSH-SST.

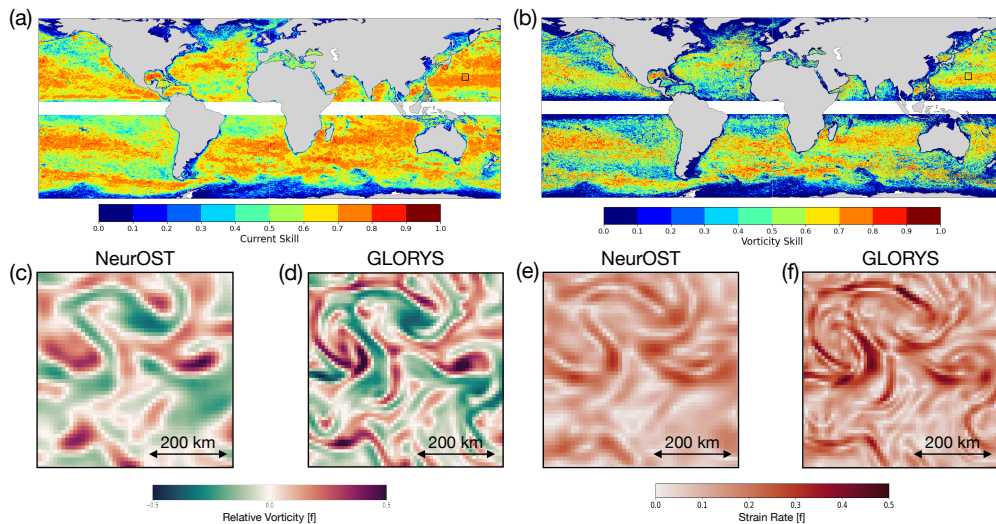


Figure 4. NeurOST SSH-SST reconstruction skill (explained variance) in GLORYS OSSE for (a) surface geostrophic currents and (b) vorticity. Snapshots of (c, d) vorticity and (e, f) strain from SNP (boxed region in a and b) for NeurOST and GLORYS on Feb 26th 2019.

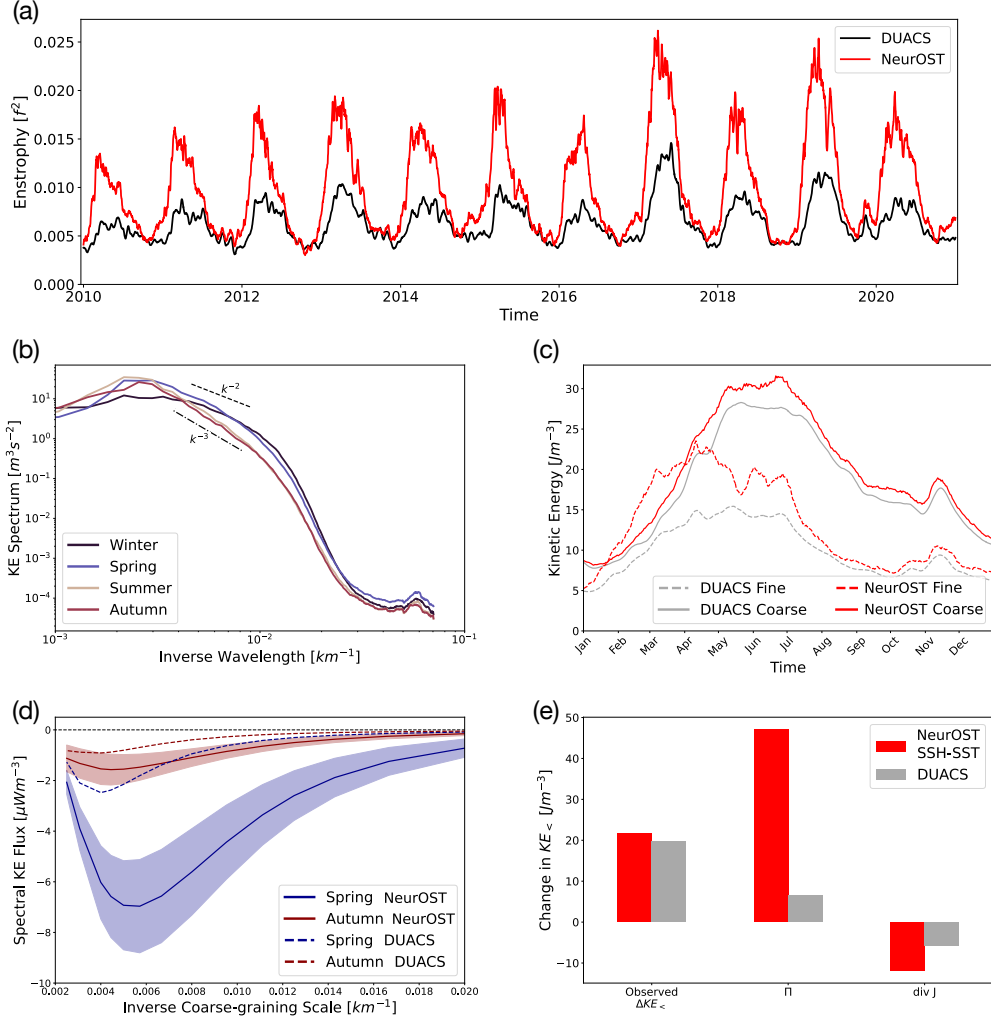


Figure 5. (a) Enstrophy time-series in the SNP for NeurOST SSH-SST and DUACS. (b) KE spectra from NeurOST SSH-SST split by season. (c) Time-series of coarse- and fine-scale KE (above and below 125km coarse-graining scale respectively) from NeurOST SSH-SST (red) and DUACS (grey). (d) KE cascade from NeurOST SSH-SST maps for the seasons of maximum (Spring) and minimum (Autumn) upscale cascade (solid line: mean, shading: standard deviation). Dashed lines are the mean cascades from DUACS. (e) Change in coarse-scale KE (KE_{\leq}) from the winter-time minimum to the summer-time maximum compared to the diagnosed contributions of the KE cascade ($-\int \Pi dt$), and the spatial transport of coarse-scale KE ($-\int \nabla \cdot J dt$) from NeurOST SSH-SST (red) and DUACS (grey) (S.I. S1.12).

References

340

- 341 Agabin, A., Prochaska, J. X., Cornillon, P. C., & Buckingham, C. E. (2023).
 342 Mitigating masked pixels in climate-critical datasets. *arXiv preprint*
 343 *arXiv:2307.09227*.
- 344 Ajayi, A., Le Sommer, J., Chassignet, E. P., Molines, J.-M., Xu, X., Albert, A., &
 345 Dewar, W. (2021). Diagnosing cross-scale kinetic energy exchanges from two
 346 submesoscale permitting ocean models. *Journal of Advances in Modeling Earth*
 347 *Systems*, *13*(6), e2019MS001923.
- 348 Aluie, H., Hecht, M., & Vallis, G. K. (2018). Mapping the energy cascade in the
 349 north atlantic ocean: The coarse-graining approach. *Journal of Physical*
 350 *Oceanography*, *48*(2), 225–244.
- 351 Arbic, B. K., Polzin, K. L., Scott, R. B., Richman, J. G., & Shriver, J. F. (2013).
 352 On eddy viscosity, energy cascades, and the horizontal resolution of gridded
 353 satellite altimeter products. *Journal of Physical Oceanography*, *43*(2), 283–
 354 300.
- 355 Archambault, T., Filoche, A., Charantonis, A., & Béréziat, D. (2024). Pre-training
 356 and fine-tuning attention based encoder decoder improves sea surface height
 357 multi-variate inpainting. In *Visapp*.
- 358 Archambault, T., Filoche, A., Charantonis, A., & Béréziat, D. (2023). Multimodal
 359 unsupervised spatio-temporal interpolation of satellite ocean altimetry maps.
 360 In *Visapp*.
- 361 Ballarotta, M., Metref, S., Albery, A., Cosme, E., Beauchamp, M., & Le Guillou,
 362 F. (2021). *Ocean data challenges*. ([https://github.com/ocean-data-
 363 -challenges/2021a_SSH_mapping_OSE](https://github.com/ocean-data-challenges/2021a_SSH_mapping_OSE))
- 364 Ballarotta, M., Ubelmann, C., Pujol, M.-I., Taburet, G., Fournier, F., Legeais, J.-F.,
 365 ... others (2019). On the resolutions of ocean altimetry maps. *Ocean Science*,
 366 *15*(4), 1091–1109.
- 367 Ballarotta, M., Ubelmann, C., Veillard, P., Prandi, P., Etienne, H., Mulet, S., ...
 368 Picot, N. (2023). Improved global sea surface height and current maps from
 369 remote sensing and in situ observations. *Earth System Science Data*, *15*(1),
 370 295–315.
- 371 Balwada, D., Xie, J.-H., Marino, R., & Feraco, F. (2022). Direct observational ev-
 372 idence of an oceanic dual kinetic energy cascade and its seasonality. *Science*
 373 *Advances*, *8*(41), eabq2566.
- 374 Beauchamp, M., Febvre, Q., Georgenthum, H., & Fablet, R. (2022). 4dvarnet-ssh:
 375 end-to-end learning of variational interpolation schemes for nadir and wide-
 376 swath satellite altimetry. *Geoscientific Model Development Discussions*, *2022*,
 377 1–37.
- 378 Buongiorno Nardelli, B., Cavaliere, D., Charles, E., & Ciani, D. (2022). Super-
 379 resolving ocean dynamics from space with computer vision algorithms. *Remote*
 380 *Sensing*, *14*(5), 1159.
- 381 Callahan, J. L., Maeda, K., & Brunton, S. L. (2019). Robust flow reconstruction
 382 from limited measurements via sparse representation. *Physical Review Fluids*,
 383 *4*(10), 103907.
- 384 Cao, Y., Dong, C., Stegner, A., Bethel, B. J., Li, C., Dong, J., ... Yang, J. (2023).
 385 Global sea surface cyclogeostrophic currents derived from satellite altimetry
 386 data. *Journal of Geophysical Research: Oceans*, *128*(1), e2022JC019357.
- 387 Carli, E., Morrow, R., Vergara, O., Chevrier, R., & Renault, L. (2023). Ocean 2d
 388 eddy energy fluxes from small mesoscale processes with swot. *Ocean Science*,
 389 *19*(5), 1413–1435.
- 390 Chelton, D. B., Ries, J. C., Haines, B. J., Fu, L.-L., & Callahan, P. S. (2001). Satel-
 391 lite altimetry. In *International geophysics* (Vol. 69, pp. 1–ii). Elsevier.
- 392 Cornillon, P. C., Firing, E., Thompson, A., Ivanov, L., Kamenkovich, I., Bucking-
 393 ham, C. E., & Afanasyev, Y. (2019). Oceans. In B. Galperin & P. Read

- 394 (Eds.), *Zonal jets phenomenology, genesis, and physics* (p. 46 - 71). Cambridge
 395 University Press. doi: 10.1017/9781107358225.003
- 396 Dufau, C., Orsztynowicz, M., Dibarboure, G., Morrow, R., & Le Traon, P.-Y.
 397 (2016). Mesoscale resolution capability of altimetry: Present and future.
 398 *Journal of Geophysical Research: Oceans*, 121(7), 4910–4927.
- 399 E.U. Copernicus Marine Service Information (CMEMS). (2024a). *Global ocean along*
 400 *track l 3 sea surface heights nrt*. Retrieved from [https://doi.org/10.48670/](https://doi.org/10.48670/moi-00147)
 401 [moi-00147](https://doi.org/10.48670/moi-00147) (Accessed on 07-04-2024)
- 402 E.U. Copernicus Marine Service Information (CMEMS). (2024b). *Global ocean along*
 403 *track l 3 sea surface heights reprocessed 1993 ongoing tailored for data assim-*
 404 *ilation*. Retrieved from <https://doi.org/10.48670/moi-00146> (Accessed on
 405 07-04-2024)
- 406 E.U. Copernicus Marine Service Information (CMEMS). (2024c). *Global ocean-*
 407 *delayed mode in situ observations of surface (drifters, hfr) and sub-surface*
 408 *(vessel-mounted adcps) water velocity*. Retrieved from [https://doi.org/](https://doi.org/10.17882/86236)
 409 [10.17882/86236](https://doi.org/10.17882/86236) (Accessed on 07-04-2024)
- 410 E.U. Copernicus Marine Service Information (CMEMS). (2024d). *Global ocean*
 411 *physics reanalysis*. Retrieved from <https://doi.org/10.48670/moi-00021>
 412 (Accessed on 07-04-2024)
- 413 Fablet, R., Amar, M. M., Febvre, Q., Beauchamp, M., & Chapron, B. (2021). End-
 414 to-end physics-informed representation learning for satellite ocean remote
 415 sensing data: Applications to satellite altimetry and sea surface currents.
 416 *ISPRS Annals of Photogrammetry, Remote Sensing & Spatial Information*
 417 *Sciences*(3).
- 418 Fablet, R., Febvre, Q., & Chapron, B. (2023). Multimodal 4dvarnets for the recon-
 419 struction of sea surface dynamics from sst-ssh synergies. *IEEE Transactions on*
 420 *Geoscience and Remote Sensing*.
- 421 Febvre, Q., Fablet, R., Le Sommer, J., & Ubelmann, C. (2022). Joint calibration
 422 and mapping of satellite altimetry data using trainable variational models. In
 423 *Icassp 2022-2022 ieee international conference on acoustics, speech and signal*
 424 *processing (icassp)* (pp. 1536–1540).
- 425 Febvre, Q., Sommer, J. L., Ubelmann, C., & Fablet, R. (2023). Training neural
 426 mapping schemes for satellite altimetry with simulation data. *arXiv preprint*
 427 *arXiv:2309.14350*.
- 428 Ferrari, R., & Wunsch, C. (2009). Ocean circulation kinetic energy: Reservoirs,
 429 sources, and sinks. *Annual Review of Fluid Mechanics*, 41, 253–282.
- 430 Fu, L.-L., Pavelsky, T., Cretaux, J.-F., Morrow, R., Farrar, J. T., Vaze, P., ... oth-
 431 ers (2024). The surface water and ocean topography mission: A breakthrough
 432 in radar remote sensing of the ocean and land surface water. *Geophysical*
 433 *Research Letters*, 51(4), e2023GL107652.
- 434 Gao, Z., Chapron, B., Ma, C., Fablet, R., Febvre, Q., Zhao, W., & Chen, G. (2024).
 435 A deep learning approach to extract balanced motions from sea surface height
 436 snapshot. *Geophysical Research Letters*, 51(7), e2023GL106623.
- 437 Garabato, A. C. N., Yu, X., Callies, J., Barkan, R., Polzin, K. L., Frajka-Williams,
 438 E. E., ... Griffies, S. M. (2022). Kinetic energy transfers between mesoscale
 439 and submesoscale motions in the open ocean’s upper layers. *Journal of Physi-*
 440 *cal Oceanography*, 52(1), 75–97.
- 441 Gaultier, L., Ubelmann, C., & Fu, L.-L. (2016). The challenge of using future swot
 442 data for oceanic field reconstruction. *Journal of Atmospheric and Oceanic*
 443 *Technology*, 33(1), 119–126.
- 444 Goh, E., Yepremyan, A. R., Wang, J., & Wilson, B. (2023). Maestro: Masked au-
 445 toencoders for sea surface temperature reconstruction under occlusion. *EGU-*
 446 *sphere*, 2023, 1–20.
- 447 Hoskins, B. J. (1982). The mathematical theory of frontogenesis. *Annual review of*
 448 *fluid mechanics*, 14(1), 131–151.

- 449 Isern-Fontanet, J., Chapron, B., Lapeyre, G., & Klein, P. (2006). Potential use of
450 microwave sea surface temperatures for the estimation of ocean currents. *Geo-*
451 *physical research letters*, *33*(24).
- 452 Isern-Fontanet, J., Shinde, M., & González-Haro, C. (2014). On the transfer func-
453 tion between surface fields and the geostrophic stream function in the mediter-
454 ranean sea. *Journal of physical oceanography*, *44*(5), 1406–1423.
- 455 Jayne, S. R., & Marotzke, J. (2002). The oceanic eddy heat transport. *Journal of*
456 *Physical Oceanography*, *32*(12), 3328–3345.
- 457 Jean-Michel, L., Eric, G., Romain, B.-B., Gilles, G., Angélique, M., Marie, D., ...
458 others (2021). The copernicus global 1/12 oceanic and sea ice glorys12 reanal-
459 ysis. *Frontiers in Earth Science*, *9*, 698876.
- 460 JPL MUR MEaSURES Project. (2015). *Ghrsst level 4 mur global foundation sea*
461 *surface temperature analysis. ver. 4.1*. Retrieved from [https://doi.org/](https://doi.org/10.5067/GHGMR-4FJ04)
462 [10.5067/GHGMR-4FJ04](https://doi.org/10.5067/GHGMR-4FJ04) (Accessed on 07-04-2024)
- 463 Klein, P., Lapeyre, G., Siegelman, L., Qiu, B., Fu, L.-L., Torres, H., ... Le Gentil, S.
464 (2019). Ocean-scale interactions from space. *Earth and Space Science*, *6*(5),
465 795–817.
- 466 Kugusheva, A., Bull, H., Moschos, E., Ioannou, A., Le Vu, B., & Stegner, A. (2024).
467 Ocean satellite data fusion for high-resolution surface current maps. *Remote*
468 *Sensing*, *16*(7), 1182.
- 469 Lagerloef, G. S., Mitchum, G. T., Lukas, R. B., & Niiler, P. P. (1999). Tropical
470 pacific near-surface currents estimated from altimeter, wind, and drifter data.
471 *Journal of Geophysical Research: Oceans*, *104*(C10), 23313–23326.
- 472 Lawrence, A., & Callies, J. (2022). Seasonality and spatial dependence of mesoscale
473 and submesoscale ocean currents from along-track satellite altimetry. *Journal of*
474 *Physical Oceanography*, *52*(9), 2069–2089.
- 475 Le Guillou, F., Gaultier, L., Ballarotta, M., Metref, S., Ubelmann, C., Cosme, E.,
476 & Rio, M.-H. (2023). Regional mapping of energetic short mesoscale ocean
477 dynamics from altimetry: performances from real observations. *Ocean Science*,
478 *19*(5), 1517–1527.
- 479 Le Guillou, F., Metref, S., Cosme, E., Ubelmann, C., Ballarotta, M., Le Sommer, J.,
480 & Verron, J. (2021). Mapping altimetry in the forthcoming swot era by back-
481 and-forth nudging a one-layer quasigeostrophic model. *Journal of Atmospheric*
482 *and Oceanic Technology*, *38*(4), 697–710.
- 483 Le Traon, P., Nadal, F., & Ducet, N. (1998). An improved mapping method of
484 multisatellite altimeter data. *Journal of atmospheric and oceanic technology*,
485 *15*(2), 522–534.
- 486 Manucharyan, G. E., Siegelman, L., & Klein, P. (2021). A deep learning approach
487 to spatiotemporal sea surface height interpolation and estimation of deep cur-
488 rents in geostrophic ocean turbulence. *Journal of Advances in Modeling Earth*
489 *Systems*, *13*(1), e2019MS001965.
- 490 Martin, S. A., Manucharyan, G. E., & Klein, P. (2023). Synthesizing sea surface
491 temperature and satellite altimetry observations using deep learning improves
492 the accuracy and resolution of gridded sea surface height anomalies. *Journal of*
493 *Advances in Modeling Earth Systems*, *15*(5), e2022MS003589.
- 494 Metref, S., & Ballarotta, M. (2023). *Ocean data challenges*. ([https://github.com/](https://github.com/ocean-data-challenges/2023a_SSH_mapping_OSE)
495 [ocean-data-challenges/2023a_SSH_mapping_OSE](https://github.com/ocean-data-challenges/2023a_SSH_mapping_OSE))
- 496 Metref, S., Ballarotta, M., Le Sommer, J., Cosme, E., Albert, A., Beauchamp,
497 M., ... Febvre, Q. (2023). *Ocean data challenges*. ([https://ocean-data-](https://ocean-data-challenges.github.io/)
498 [challenges.github.io/](https://ocean-data-challenges.github.io/))
- 499 Morrow, R., Fu, L.-L., Arduin, F., Benkiran, M., Chapron, B., Cosme, E., ... oth-
500 ers (2019). Global observations of fine-scale ocean surface topography with
501 the surface water and ocean topography (swot) mission. *Frontiers in Marine*
502 *Science*, *6*, 232.
- 503 Penven, P., Halo, I., Pous, S., & Marié, L. (2014). Cyclogeostrophic balance in the

- 504 mozambique channel. *Journal of Geophysical Research: Oceans*, 119(2), 1054–
505 1067.
- 506 Qiu, B., Chen, S., Klein, P., Sasaki, H., & Sasai, Y. (2014). Seasonal mesoscale and
507 submesoscale eddy variability along the north pacific subtropical countercur-
508 rent. *Journal of Physical Oceanography*, 44(12), 3079–3098.
- 509 Rio, M.-H., Mulet, S., & Picot, N. (2014). Beyond goce for the ocean circulation es-
510 timate: Synergetic use of altimetry, gravimetry, and in situ data provides new
511 insight into geostrophic and ekman currents. *Geophysical Research Letters*,
512 41(24), 8918–8925.
- 513 Rio, M.-H., Santoleri, R., Bourdalle-Badie, R., Griffa, A., Piterbarg, L., & Taburet,
514 G. (2016). Improving the altimeter-derived surface currents using high-
515 resolution sea surface temperature data: a feasibility study based on model
516 outputs. *Journal of Atmospheric and Oceanic Technology*, 33(12), 2769–2784.
- 517 Sasaki, H., Klein, P., Qiu, B., & Sasai, Y. (2014). Impact of oceanic-scale inter-
518 actions on the seasonal modulation of ocean dynamics by the atmosphere. *Na-
519 ture communications*, 5(1), 5636.
- 520 Schubert, R., Gula, J., Greatbatch, R. J., Baschek, B., & Biastoch, A. (2020). The
521 submesoscale kinetic energy cascade: Mesoscale absorption of submesoscale
522 mixed layer eddies and frontal downscale fluxes. *Journal of Physical Oceanog-
523 raphy*, 50(9), 2573–2589.
- 524 Schubert, R., Vergara, O., & Gula, J. (2023). The open ocean kinetic energy cascade
525 is strongest in late winter and spring. *Communications Earth & Environment*,
526 4(1), 450.
- 527 Scott, R. B., & Wang, F. (2005). Direct evidence of an oceanic inverse kinetic en-
528 ergy cascade from satellite altimetry. *Journal of Physical Oceanography*, 35(9),
529 1650–1666.
- 530 Siegelman, L., Klein, P., Rivière, P., Thompson, A. F., Torres, H. S., Flexas, M., &
531 Menemenlis, D. (2020). Enhanced upward heat transport at deep submesoscale
532 ocean fronts. *Nature Geoscience*, 13(1), 50–55.
- 533 Sinha, A., & Abernathey, R. (2021). Estimating ocean surface currents with machine
534 learning. *Frontiers in Marine Science*, 8, 672477.
- 535 Steinberg, J. M., Cole, S. T., Drushka, K., & Abernathey, R. P. (2022). Seasonality
536 of the mesoscale inverse cascade as inferred from global scale-dependent eddy
537 energy observations. *Journal of Physical Oceanography*, 52(8), 1677–1691.
- 538 Storer, B. A., & Aluie, H. (2023). Flowsieve: A coarse-graining utility for geophys-
539 ical flows on the sphere. *Journal of Open Source Software*, 8(84), 4277.
- 540 Storer, B. A., Buzzicotti, M., Khatri, H., Griffies, S. M., & Aluie, H. (2022). Global
541 energy spectrum of the general oceanic circulation. *Nature communications*,
542 13(1), 5314.
- 543 Storer, B. A., Buzzicotti, M., Khatri, H., Griffies, S. M., & Aluie, H. (2023). Global
544 cascade of kinetic energy in the ocean and the atmospheric imprint. *arXiv
545 preprint arXiv:2311.09100*.
- 546 Taburet, G., Sanchez-Roman, A., Ballarotta, M., Pujol, M.-I., Legeais, J.-F.,
547 Fournier, F., . . . Dibarboure, G. (2019). DUACS DT2018: 25 years of re-
548 processed sea level altimetry products. *Ocean Science*, 15(5), 1207–1224.
- 549 Thiria, S., Sorrow, C., Archambault, T., Charantonis, A., Bereziat, D., Mejia, C., . . .
550 Crépon, M. (2023). Downscaling of ocean fields by fusion of heterogeneous
551 observations using deep learning algorithms. *Ocean Modelling*, 182, 102174.
- 552 Torres, H. S., Klein, P., Menemenlis, D., Qiu, B., Su, Z., Wang, J., . . . Fu, L.-L.
553 (2018). Partitioning ocean motions into balanced motions and internal gravity
554 waves: A modeling study in anticipation of future space missions. *Journal of
555 Geophysical Research: Oceans*, 123(11), 8084–8105.
- 556 Ubelmann, C., Carrere, L., Durand, C., Dibarboure, G., Faugère, Y., Ballarotta, M.,
557 . . . Lyard, F. (2022). Simultaneous estimation of ocean mesoscale and coherent
558 internal tide sea surface height signatures from the global altimetry record.

- 559 *Ocean Science*, 18(2), 469–481.
- 560 Ubelmann, C., Dibarboure, G., Gaultier, L., Ponte, A., Ardhuin, F., Ballarotta, M.,
561 & Faugère, Y. (2021). Reconstructing ocean surface current combining alti-
562 metry and future spaceborne doppler data. *Journal of Geophysical Research:*
563 *Oceans*, 126(3), e2020JC016560.
- 564 Ubelmann, C., Klein, P., & Fu, L.-L. (2015). Dynamic interpolation of sea surface
565 height and potential applications for future high-resolution altimetry mapping.
566 *Journal of Atmospheric and Oceanic Technology*, 32(1), 177–184.
- 567 Uchida, T., Abernathy, R., & Smith, S. (2017). Seasonality of eddy kinetic energy
568 in an eddy permitting global climate model. *Ocean Modelling*, 118, 41–58.
- 569 Wang, H., Grisouard, N., Salehipour, H., Nuz, A., Poon, M., & Ponte, A. L. (2022).
570 A deep learning approach to extract internal tides scattered by geostrophic
571 turbulence. *Geophysical Research Letters*, 49(11), e2022GL099400.
- 572 Wunsch, C. (1999). Where do ocean eddy heat fluxes matter? *Journal of Geophys-*
573 *ical Research: Oceans*, 104(C6), 13235–13249.
- 574 Xiao, Q., Balwada, D., Jones, C. S., Herrero-González, M., Smith, K. S., & Aber-
575 nathey, R. (2023). Reconstruction of surface kinematics from sea surface
576 height using neural networks. *Journal of Advances in Modeling Earth Systems*,
577 15(10), e2023MS003709.
- 578 Zhang, Z., Wang, W., & Qiu, B. (2014). Oceanic mass transport by mesoscale ed-
579 dies. *Science*, 345(6194), 322–324.

Supporting Information for "Deep Learning Improves Global Satellite Observations of Ocean Eddy Dynamics"

Scott A. Martin¹, Georgy E. Manucharyan¹, and Patrice Klein^{2,3}

¹School of Oceanography, University of Washington, Seattle, WA, USA

²Jet Propulsion Laboratory, California Institute of Technology, Pasadena, CA, USA

³Laboratoire de Météorologie Dynamique, École Normale Supérieure, Paris, France

Contents of this file

1. Text S1 to S2
2. Tables S1 to S4
3. Figures S1 to S9

Additional Supporting Information (Files uploaded separately)

1. Caption for Movie S1

1. Text S1: Extended Methods

1.1. Sea surface height and surface geostrophic currents

At large temporal and spatial scales, ocean currents are approximately in geostrophic balance (Vallis, 2017), meaning that currents arrange themselves such that the horizontal pressure gradient force is balanced by the Coriolis force. Surface pressure in the ocean can be directly related to sea surface height anomaly (SSH), allowing surface current velocity to be estimated from satellite altimeter observations of SSH. The surface currents are proportional to the spatial gradients of the SSH field

$$(u_g, v_g) = \frac{g}{f} \left(-\frac{\partial \eta}{\partial y}, \frac{\partial \eta}{\partial x} \right), \quad (1)$$

where u_g and v_g are the Eastward and Northward geostrophic surface currents respectively, g is the acceleration due to gravity, η is the SSH, f is the local Coriolis frequency, and x and y are zonal and meridional coordinates respectively. This relation breaks down near the Equator where f approaches zero, so we do not calculate surface geostrophic currents within the equatorial band (5°S to 5°N).

Geostrophy breaks down at smaller scales where the impact of non-linear advection becomes significant, and does not account for wind-induced Ekman currents. Empirical corrections can be made to geostrophy at the Equator (Lagerloef et al., 1999), to estimate Ekman currents (Rio et al., 2014), and to include the effect of non-linear advection through cyclo-geostrophic balance (Penven et al., 2014; Cao et al., 2023). Ekman currents and equatorial dynamics are not the focus of this study, but since cyclo-geostrophy is pertinent for mesoscale eddies we do assess the sensitivity of our results to correcting

for this component using the iterative method proposed in Penven et al. (2014). The cyclo-geostrophic correction leads to a marginally improved surface current RMSE when evaluated using drifters compared to conventional geostrophy but the change is typically well below 10%, highlighting the relatively small impact of this correction at the scales resolved here (S.I. Figure 2). Further, we find that the KE cascade diagnosed from both NeurOST and GLORYS changes very little when the cyclo-geostrophic correction is applied (S.I. Figure 2). The near-perfect agreement between the GLORYS cyclo-geostrophic KE cascade and that from the GLORYS 15m currents highlights the pertinence of this empirical correction, but the small correction to the currents highlights that they are to leading order geostrophic.

1.2. Satellite datasets

The along-track SSH observations used in this study are those processed by the Data Unification and Altimeter Combination System (DUACS) and distributed by the Copernicus Marine Environmental Service (CMEMS) (E.U. Copernicus Marine Service Information (CMEMS), 2024b, 2024a). Specifically, we use the unfiltered, Level 3 sea level anomaly observations. At Level 3, the observations have been corrected for atmospheric effects, the barotropic tide has been removed, and the data has been adjusted to ensure consistency between the different altimeter missions.

We use the Multi-scale Ultra-high Resolution (MUR) SST analysis product to provide a gridded estimate of SST as an additional predictor variable in the mapping of SSH that combines observations from a wide range of satellite infrared and microwave radiometer observations (JPL MUR MEaSURES Project, 2015; Chin et al., 2017). While this product

is distributed on a 1/100th degree grid, the spatial scales resolved vary in space and time due to satellite sampling and cloud cover.

1.3. Formulating SSH interpolation as a self-supervised deep learning problem

After appropriate data pre-processing, SSH interpolation can be viewed as a video inpainting problem with an extremely high missing pixel rate ($\sim 90\%$) (Manucharyan et al., 2021; Martin et al., 2023; Fablet et al., 2021). We first extract satellite altimeter SSH observations in some restricted spatiotemporal subdomain within which we seek to estimate the full SSH field. This subdomain is discretized into a regular grid in space and time onto which the observations are bin-averaged; empty voxels are padded with zeroes. This data can now be considered as a heavily-masked video, and our objective is to predict the corresponding full, unmasked video using a deep learning neural network. The objective minimised during training is the mean squared error (MSE) between the prediction and the ground-truth. When training on real-world altimetry observations, there is no full unmasked ground-truth dataset to use during training. We overcome this by randomly withholding some of the altimetry observations from the input and calculating the MSE only at the locations of these withheld observations (Martin et al., 2023). Co-located estimates of gridded SST are used as an extra predictor variable by averaging them onto the same local grid and presenting this (unmasked) video as an additional input to the neural network. The dimensions of the local grid on which we map SSH were chosen to be 128x128 in the spatial domain with 7.5km grid resolution (latitude, longitude coordinates are first projected onto a local orthonormal grid to avoid distortion), and 30 frames in the temporal domain with 1 day grid resolution. Rationalisation and

validation of these choices is given in our previous study (Martin et al., 2023). To train our network, we generated a training dataset of 1 million local subdomains centred on random points in space and time throughout the Global Ocean. The data are split in the temporal domain to ensure well-separated training, validation, and testing datasets, with 2019 being withheld for testing, and the remaining years from 2010-2022 split into non-overlapping training and validation periods (S.I. Figure 2).

The mapping errors grow away from the centre of the local spatiotemporal grid due the omission of observations outside the local subdomain, therefore to produce the optimal reconstruction we use only the middle day of the predicted time-series during inference and points close to the edge of the subdomain are given low weight in our algorithm for merging subdomain reconstructions to produce a global SSH estimate 1.5.

1.4. Deep learning neural network architecture

After formulating SSH interpolation as discussed above, we are free to use any sequence-to-sequence video prediction model from the extensive computer vision literature. To ensure we employed a state-of-the-art architecture, we chose the top-performing architecture on the Moving MNIST video prediction benchmark (Srivastava et al., 2015) at the time of our study, SimVP (Gao et al., 2022; Tan et al., 2022). SimVP is built up of three modules: a spatial encoder that learns to encode each frame of the input independently in some lower-dimensional latent space, a temporal translator that learns both spatial and temporal dependencies from the latent space, and a spatial decoder that decodes the latent space into the predicted video frames. Unlike widely-used recurrent architectures, such as ConvLSTM (Shi et al., 2015), SimVP uses convolutional neural net-

works (CNNs) for all three modules. Our architecture is as described in Tan et al. (Tan et al., 2022), where the temporal translator module is a gated spatio-temporal attention translator, which uses large convolutional kernels to imitate the attention mechanism allowing the translator to adaptively select informative features from the latent space. Compared with Tan et al., we removed the skip connection from the first layer of the spatial encoder to the final layer of the spatial decoder since the extreme sparsity of the input SSH frames led to the appearance of artifacts in the output coinciding with the input altimeter tracks. To synthesise SSH and SST, we use a separate spatial encoder for each variable before concatenating the encoded SSH and SST in the channel dimension and passing this to the temporal translator. Except for the temporal translator, the architecture used here is similar to the ConvLSTM-based architecture used in our earlier regional SSH mapping study (Martin et al., 2023). During early testing we found SimVP to outperform ConvLSTM in global SSH reconstruction, which requires a more expressive architecture due to the diverse range of dynamical regimes, and its performance (when trained on global data) is comparable to our previously published values for ConvLSTM in the Gulf Stream despite the latter being trained exclusively on this region (S.I. Table 2). Each network was trained for 50 epochs using the OneCycle learning rate scheduling policy, the Adam optimiser, and with drop-out and drop-path probabilities of 0.2 and 0.15 respectively which were selected after performing hyper-parameter optimisation on 10% of the training data. Each training on the global training dataset took 7 days on a single node with four Nvidia V100 GPUs.

1.5. Merging subdomain reconstructions to create global SSH product

Our neural network predicts gridded SSH on subdomains of size 960x960km. To produce a global gridded SSH estimate we use the trained network to predict SSH on 5615 subdomains with centres chosen to be approximately equally spaced by a distance of 250km throughout the Global Ocean. There is therefore substantial overlap between neighbouring subdomains. To merge the subdomain reconstructions into a single global SSH estimate we use the kernel-weighted averaging method described in Appendix A of Callaham et al. (Callaham et al., 2019) and outlined below.

The global 2D SSH estimate, $\hat{\mathbf{x}}$, defined on a regular 1/10th degree grid, is computed from the k subdomain estimates through

$$\hat{\mathbf{x}} = \sum_{i=1}^k \Phi_i \odot \hat{\mathbf{x}}_i, \quad (2)$$

where Φ_i is a normalised weighting kernel for each subdomain, $\hat{\mathbf{x}}_i$ are the subdomain SSH estimates, and \odot denotes the Hadamard (i.e. element-wise) product between two matrices. Note that each $\hat{\mathbf{x}}_i$ and Φ_i are filled with zeroes at all points covered by land or sea ice and at points lying outside the subdomain. All matrices were first regridded to the regular 1/10th degree grid from the original, irregular subdomain grid using bilinear interpolation. Each weighting kernel is taken to be a Gaussian centred on the corresponding subdomain

$$\Phi_i(\mathbf{r}) = \frac{1}{N(\mathbf{r})} \exp\left(-\frac{|\mathbf{r} - \mathbf{r}_i|^2}{L^2}\right), \quad (3)$$

where \mathbf{r} is the position of the point being estimated, \mathbf{r}_i is the position of the subdomain centre, L is the characteristic width of the Gaussian kernel, and $N(\mathbf{r})$ is a normalisation

factor chosen such that

$$N(\mathbf{r}) = \sum_{i=1}^k \Phi_i(\mathbf{r}). \quad (4)$$

The mapping errors in the subdomain reconstructions are expected to increase away from the centre of the subdomain due to the omission of observations outside the subdomain in the mapping. Thus, for minimising the error of the global estimate maximising the number of subdomains is desirable. The choice to space the subdomains by 250km was made as the minimum spacing our computing resources would reasonably permit (merging the subdomain reconstructions for a single day takes ~ 3 minutes per CPU worker at this spacing). Given this subdomain spacing, the value of L was tuned so as to minimise the mapping error for the global estimate. We found the errors to be only weakly dependent on kernel width for widths within reasonable bounds, the results presented in the manuscript were obtained using $L = 250\text{km}$. All first- and second-order spatial derivatives of the SSH field were computed first on the orthonormal subdomain grid using smooth noise-robust differentiator kernels (discussed in Arbic et al. (Arbic et al., 2012)) before being merged using the above algorithm to avoid the appearance of high-frequency numerical artefacts (Martin et al., 2023) (a similar result can be obtained by a simple low-pass filtering of the mapped SSH).

1.6. Regional fine-tuning experiment

In S.I. Table 2 we show that NeurOST SSH-SST trained on global observations can be fine-tuned for regional applications to bring its performance closer to that of state-of-the-art regional schemes (Febvre et al., 2023; Martin et al., 2023). The global model was trained on 1 million training examples drawn randomly from the Global Ocean. During

fine-tuning we started training from the converged global model using the Adam optimiser with a fixed learning rate parameter of 10^{-4} on a smaller training set of 100 thousand examples drawn randomly from the Gulf Stream (as in our previous study (Martin et al., 2023)) and continued training until the validation loss stopped improving. This fine-tuning took 12 hours on a single node with four Nvidia V100 GPUs. The results presented in the rest of the study use only the global trained model to limit the computational resources of the method, but in future an ensemble of bespoke regional models could be fine-tuned to further optimise the SSH mapping in each region if these maps were produced operationally by a data centre. Since previous studies used a different test year, 2017, in the Gulf Stream (Ballarotta et al., 2021), we swapped 2017 and 2019 in our training-validation-testing split (S.I. Figure 2) to ensure 2017 was withheld during training and cross-validation (both the global and regional training were done with this updated split).

1.7. SSH map evaluation and inter-comparison OSE

To evaluate the accuracy and resolution of the SSH signals resolved by different mapping methods, we employ an ‘observing system experiment’ (OSE) in which each method is used to generate global gridded SSH estimates using all but one of the available satellite altimeters which is then used as an independent validation of the mapped signal. Since the existing operational SSH products are only distributed using all available altimeters, performing an OSE would typically involve re-implementation of all existing methods, which would be challenging in the case of SSH mapping since the covariance parameters used to create the community-standard DUACS product are not publicly-available. To address this, in recent years a series of ‘Ocean Data Challenges’ have been developed

(Metref et al., 2023). In each challenge a common mapping OSE problem is defined, developers of different methods implement their method and post their results, allowing a transparent performance benchmark.

To evaluate our global product, we use the recently-created global OSE challenge: ‘2023a_SSH_mapping_OSE’ (Metref & Ballarotta, 2023). In this challenge, each method is used to create 1 year (2019) of global gridded SSH estimates using SSH observations from the satellites Jason 3, Sentinel 3A, Sentinel 3B, Haiyang-2A, Haiyang-2B, and Cryosat-2, while observations from the satellite Saral/Altika are withheld for validation. While the validation observations only sample the maps along 1D tracks, aggregating over a full year allows robust, geographically-varying error statistics to be found.

We present three SSH error metrics using the withheld altimeter, each averaged over the full year and binned into 1° bins: the root-mean-square error (RMSE) between the mapped and observed signals, the RMSE after applying a 70-250km along-track band-pass spatial filter to both the observed and mapped signals along the satellite tracks to highlight the maps’ ability to map small mesoscale eddies, and the effective spatial resolution of the mapped signal. The effective resolution is found by taking along-track segments of the withheld altimeter observations along with the mapped values at these locations and calculating the signal-to-noise ratio as a function of wavelength by dividing the power spectral density of the mapping errors by that of the observations. Concretely, the ‘effective spatial resolution’ is taken to be the wavelength at which the signal-to-noise ratio between the observed and mapped signals drops below 0.5 (Ballarotta et al., 2019).

To evaluate the surface currents inferred from each SSH map, surface drifter observations from the CMEMS global in-situ water velocity product (E.U. Copernicus Marine Service Information (CMEMS), 2024c) are used. Surface drifter observations are not used in the generation of any of the surface current maps presented here, so they are an independent validation dataset. We present geographically averaged velocity RMSE values for each method.

At the time of writing, three other SSH mapping methods have been implemented worldwide and all are available in the data challenge for evaluation: DUACS (Le Traon et al., 1998; Taburet et al., 2019), MIOST (geostrophic) (Ubelmann et al., 2021), and MIOST (geostrophic + equatorial waves) (Ballarotta et al., 2023). DUACS (Data Unification and Altimeter Combination Service) is the community-standard gridded SSH product that is distributed operationally by CMEMS. The DUACS system uses a linear optimal interpolation (OI) formulation (Bretherton et al., 1976), in which an *a priori* model is prescribed for how SSH covaries in space and in time, then the missing values are estimated using the best linear least-squares estimator. The assumed covariance, C , is

$$C(r, t) = \left(1 + ar + \frac{1}{6}(ar)^2 - \frac{1}{6}(ar)^3\right) \exp(-ar) \exp\left(\frac{-t^2}{T^2}\right), \quad (5)$$

where t is the temporal separation of the observation and mapped point under consideration, T is a prescribed de-correlation time-scale, $a = 3.337$, and

$$r = \sqrt{\left(\frac{dx - C_{px}t}{L_x}\right)^2 + \left(\frac{dy - C_{py}t}{L_y}\right)^2}, \quad (6)$$

where L_x and L_y are prescribed de-correlation length-scales in the zonal and meridional directions, dx and dy are respectively the zonal and meridional separation of the observa-

tion and mapped point under consideration, and C_{px} and C_{py} are prescribed propagation velocities. The de-correlation scales and propagation velocities are allowed to vary with geographical location and the values used are not publicly available but have been tuned over many years to best map mesoscale ocean features globally. The MIOST (Multiscale Interpolation Ocean Science Topography) mapping method extends the linear mapping framework, using a wavelet decomposition to allow the construction of multiple independent components of the assumed covariance model (Ubelmann et al., 2022; Ballarotta et al., 2023). MIOST (geostrophic) uses a single component in the covariance model intended to represent the geostrophically balanced component of SSH evolution, while MIOST (geostrophy + equatorial waves) adds an additional component to model the propagation of tropical instability waves and Poincare waves near the equator.

1.8. Season definitions

Wherever results are split by season in this study we define those seasons in the Northern (Southern) Hemisphere: winter is January-March (July-September), spring is April-June (October-December), summer is July-September (January-March), and autumn is October-December (April-June).

1.9. Eddy kinetic energy

The kinetic energy, KE, per unit volume of the surface currents is calculated from the surface geostrophic current maps

$$\text{KE} = \frac{\rho_0}{2} (u_g^2 + v_g^2), \quad (7)$$

where ρ_0 is a reference density taken to be 1025kgm^{-3} . The eddy kinetic energy, EKE, is defined as the time-varying component of the KE

$$\text{EKE} = \text{KE} - \overline{\text{KE}}, \quad (8)$$

where $\overline{\text{KE}}$ is the time mean of the KE.

To highlight the difference in small-scale EKE between the maps we also calculate the EKE of the surface currents after the application of a 250km high-pass filter.

1.10. Relative vorticity, strain rate, and Okubo-Weiss quantity

While first order spatial derivatives of SSH give the velocity of the geostrophic currents, second order spatial derivatives quantify the deformation and rotation induced by the flow. The relative vorticity, ω , describes the local rotation of the fluid (that is, how a patch of tracers would tend to rotate if placed at a point within the flow)

$$\omega = \frac{\partial v_g}{\partial x} - \frac{\partial u_g}{\partial y} = \frac{g}{f} \nabla_h^2 \eta, \quad (9)$$

where ∇_h^2 is the horizontal Laplacian.

Meanwhile, the strain rate, s , defines the deformation of fluid elements by the flow (that is, how a patch of tracers would change shape due to the flow)

$$s = \sqrt{s_n^2 + s_s^2} \quad (10)$$

where s_n is the normal component of the strain

$$s_n = \frac{\partial u_g}{\partial x} - \frac{\partial v_g}{\partial y} = -2 \frac{g}{f} \frac{\partial^2 \eta}{\partial x \partial y}, \quad (11)$$

and s_s is the shear component

$$s_s = \frac{\partial v_g}{\partial x} + \frac{\partial u_g}{\partial y} = \frac{g}{f} \left(\frac{\partial^2 \eta}{\partial x^2} - \frac{\partial^2 \eta}{\partial y^2} \right). \quad (12)$$

A high strain rate is associated with the stretching of patches of fluid, is common in the areas between eddies, and is associated with the generation of submesoscale filaments through frontogenesis (Hoskins, 1982) and strong transfer of kinetic energy between scales (Aluie et al., 2018). Whereas strong relative vorticity (either positive or negative) is associated with coherent, persistent eddies and is typical in the cores of eddies.

The relative importance of relative vorticity and strain rate at each point in the fluid can be described using the Okubo-Weiss quantity (Okubo, 1970; Weiss, 1991),

$$W = s^2 - \omega^2, \quad (13)$$

which is positive when strain dominates and negative when relative vorticity dominates (Figure 3 in main text).

1.11. Eddy Dynamics Evaluation OSSE

As described in the main text, we use the GLORYS reanalysis product to implement an OSSE to evaluate the realism of eddy dynamics by generating synthetic altimetry observations from the reanalysis and inputting them to NeurOST. To ensure consistency with our OSE, we use 2019 as the test year and sample the GLORYS SSH along the locations of the 2019 altimeter tracks, applying regionally-varying white noise consistent with that described in the user guide for the along-track SSH observations (E.U. Copernicus Marine Service Information (CMEMS), 2024b, 2024a).

The metrics we use to evaluate the realism of the mapped surface currents and vorticity normalized skill scores that give the fraction of variance explained.

For surface currents this skill is defined as

$$\text{skill} = 1 - \frac{\text{MSE}(u_g) + \text{MSE}(v_g)}{\text{Var}(u_g) + \text{Var}(v_g)}, \quad (14)$$

where MSE is mean squared error and Var is the variance. Similarly for relative vorticity, ζ_g , this is defined as

$$\text{skill} = 1 - \frac{\text{MSE}(\zeta_g)}{\text{Var}(\zeta_g)}. \quad (15)$$

1.12. KE cascade: diagnosing energy transfer between scales

Energy transfers between flows of different length-scales, a characteristic property of turbulent flows, can be diagnosed using a coarse-graining analysis (Aluie et al., 2018). By applying convolutions to the Navier-Stokes equation and neglecting small contributions from molecular viscosity, a kinetic energy (KE) budget for the coarse-grained flow (i.e. the velocity after convolution with a smoothing filter) is obtained (Aluie et al., 2018)

$$\frac{\partial}{\partial t} \rho_0 \frac{|\bar{\mathbf{u}}_l|^2}{2} = -\nabla \cdot \mathbf{J}_l^{\text{transport}} - \Pi_l + \bar{\rho}_l \mathbf{g} \cdot \bar{\mathbf{u}}_l + \rho_0 \bar{\mathbf{F}}_l^{\text{forcing}} \cdot \bar{\mathbf{u}}_l, \quad (16)$$

where $\bar{\cdot}_l$ represents convolution with a filter with scale diameter l , $\mathbf{J}_l^{\text{transport}}$ is the spatial transport of large-scale KE (as defined in ref (Aluie et al., 2018)), ρ_0 is a reference density (here taken to be 1025kgm^{-3}), Π_l is the transfer of energy between scales by non-linear eddy interactions defined below, \mathbf{g} is the acceleration due to gravity, and $\bar{\mathbf{F}}_l^{\text{forcing}}$ is any external forcing at scales above l (e.g. by winds). The third term on the right represents the conversion of potential energy into kinetic.

The existence of an upscale (or ‘inverse’) cascade of KE is a characteristic property of geophysical turbulence (Vallis, 2017) that is hypothesised to play a role in setting the seasonality of mesoscale ocean eddies (Sasaki et al., 2014; Qiu et al., 2014). We therefore

here diagnose the transfer of KE between scales, Π_l , from surface geostrophic current maps to assess its magnitude and sign at different spatial scales, implicitly neglecting energy associated with vertical velocities (which are small at the scales considered here). We don't seek to close the energy budget in Equation 16 as this would require precise determination of the potential energy conversion and external forcing at the same resolution as the surface geostrophic current maps.

The KE cascade, Π_l , is caused by non-linear interactions between eddies and is characterised by the interplay between the large-scale strain tensor, $\bar{\mathbf{S}}_l$, and the subfilter-scale stress, $\bar{\tau}_l$, through (Aluie et al., 2018)

$$\Pi_l = -\rho_0 \bar{S}_{ij} \bar{\tau}_{ji}, \quad (17)$$

where

$$\bar{S}_{ij} = \frac{1}{2} (\partial_i \bar{u}_j + \partial_j \bar{u}_i), \quad (18)$$

$$\bar{\tau}_{ij} = \overline{u_i u_j} - \bar{u}_i \bar{u}_j, \quad (19)$$

repeated indices are summed over, and the subscript l in the coarse-graining operation has been dropped when using index notation to avoid confusion between the coarse-graining length scale and a spatial index. The cascade term, Π_l , represents the energy transfer from scales larger than l to smaller scales due to non-linear eddy interactions, so Π_l is positive (negative), energy is transferred from scales larger (smaller) than l to smaller (larger) scales representing a downscale (upscale) cascade. Scrutiny of Equation 17 highlights the sensitivity of the KE cascade to the strain rate, and hence to eddy geometry.

We use an open-source code, FlowSieve (Storer & Aluie, 2023), to coarse-grain the surface geostrophic current maps at a range of scales, l , and diagnose Π_l and $\mathbf{J}_l^{\text{transport}}$.

While this coarse-graining can be done on global surface current fields accounting for the spherical geometry of the Earth's surface (Storer & Aluie, 2023), we here restrict our attention to a selection of open ocean regions (defined in S.I. Table 2). This prevents the need to prescribe boundary conditions at coastlines and significantly reduces the computational requirements of the analysis. All velocities are first projected onto a local ortho-normal grid with a grid spacing 10km and side length of 2560km. We perform coarse-graining on this grid and diagnose Π_l and $\mathbf{J}_l^{\text{transport}}$ as a function of l and time at each grid point, before taking a spatial average of both quantities over a smaller box in the centre of the domain with side length 1280km. The smoothing filter used in the coarse-graining is a smoothed top-hat, as used in previous studies (Storer et al., 2022)

$$G_l(\mathbf{r}) = \frac{A}{2} \left(1 - \tanh \left[10 \left(\frac{|\mathbf{r}|}{l/2} - 1 \right) \right] \right), \quad (20)$$

where A is a normalisation calculated numerically to ensure G_l integrates to unity and \mathbf{r} is the separation between the evaluation point and the centre of the convolutional kernel. The coarse-grained fields, $\bar{f}_l(\mathbf{x})$, are then defined as

$$\bar{f}_l(\mathbf{x}) = G_l * f, \quad (21)$$

where $*$ is a two-dimensional convolution.

There is no direct correspondence between the filter scales, l , used in coarse-graining and wavelengths in a Fourier analysis (e.g. the KE spectra in Figure 5 in the Main Text). To aid interpretation of the coarse-graining results in comparison to the spectral analysis we used to evaluate the effective resolution of each SSH map, we empirically calculate associated effective coarse-graining scales for each SSH map (method described below).

When assessing the ability of the KE cascade to drive the summer-time peak in large-scale KE, we compare the change in large-scale KE from its winter minimum to its summer maximum to the time integrals of $(-\Pi_l)$ and $(-\nabla \cdot \mathbf{J}_l^{\text{transport}})$ over the same time period. This analysis neglects sources/sinks of energy at larger scales, energy lost from surface currents due to eddy barotropisation, and conversion of potential energy to KE but in this study we don't seek to close the large-scale KE budget, merely to demonstrate that the diagnosed Π_l is greatly changed between maps and that its strength becomes large enough to be a significant contributor to the change in large-scale KE.

1.13. KE Wavenumber Spectrum Calculation

To calculate the KE wavenumber spectra in Figure 5 of the main text we calculated 2D KE wave-number spectra on a local, ortho-normal grid and azimuthally averaged to collapse the meridional and zonal dimensions into a single wavenumber.

2. Text S2: Effective coarse-graining scale of SSH maps

To aid interpretation of the effective resolution metric (Ballarotta et al., 2019), we also provide a corresponding 'effective coarse-graining scale'. This metric can be interpreted as the coarse-graining scale that best represents the smoothing induced by the SSH mapping algorithm and is useful when considering our KE cascade results which were obtained using coarse-graining.

The effective coarse-graining scale is obtained by positing that the mapped signal can reasonably be approximated as a coarsened version of the true signal where a smoothing kernel has been convolved with the observations.

For a mapped along-track signal x , and an observed signal y , the effective resolution is defined (Ballarotta et al., 2019) as the wavelength where the function, f , crosses 0.5, where

$$f(k) = 1 - \frac{(\widehat{x - y})^* (\widehat{x - y})}{\widehat{y}^* \widehat{y}}, \quad (22)$$

where $*$ represents complex conjugation, a "hat" is the Fourier transform, and k is the along-track wavenumber.

We suppose that the mapped signal, x , can be approximated as the convolution of y with a smoothing kernel, G_l , with corresponding spatial scale, l ,

$$x = G_l * y. \quad (23)$$

Using the convolution theorem and plugging this definition of x into Equation 22 yields an expression for f in terms of the smoothing kernel

$$f(k) = \widehat{G}_l + \widehat{G}_l^* - \widehat{G}_l^* \widehat{G}_l. \quad (24)$$

For any given kernel, G_l , its Fourier transform, and hence $f(k)$, depends only on the coarse-graining scale, l . Thus for each map and region we fit the function in Equation 24 to the data for $f(k)$ for different coarse-graining kernels, G_l , to find corresponding coarse-graining scales, l . We refer to the resulting scale as the 'effective coarse-graining scale' of the SSH map for each kernel.

In S.I. Table 2, we compare the effective resolution to the effective coarse-graining scales for a Gaussian kernel

$$G_l^{\text{Gaussian}}(x - x') = \frac{1}{l\sqrt{2\pi}} \exp\left(-\frac{|x - x'|^2}{2l^2}\right), \quad (25)$$

and the smooth top-hat kernel

$$G_l^{\text{FlowSieve}}(x - x') = \frac{A}{2} \left(1 - \tanh \left[10 \left(\frac{|x - x'|}{l/2} - 1 \right) \right] \right), \quad (26)$$

used in FlowSieve (Storer & Aluie, 2023) that we used to diagnose the energy transfer between scales, where $|x - x'|$ is the distance between the analysis point and the kernel centre and A is a normalisation factor computed numerically. Note that for $G_l^{\text{FlowSieve}}$ the Fourier transform becomes oscillatory at high wavenumbers, we therefore set all values of the fitted $f(k)$ to zero at wavenumbers past the first zero crossing to ensure we only fit the physically meaningful part of the curve to the data.

Movie S1. Movie of relative vorticity in the Subtropical North Pacific (150-160°W, 20-30°N) from NeurOST SSH-SST (captioned ‘SimVP SSH-SST’ in the movie in reference to the neural network architecture) and DUACS.

References

- Aluie, H., Hecht, M., & Vallis, G. K. (2018). Mapping the energy cascade in the north atlantic ocean: The coarse-graining approach. *Journal of Physical Oceanography*, *48*(2), 225–244.
- Arbic, B. K., Scott, R. B., Chelton, D. B., Richman, J. G., & Shriver, J. F. (2012). Effects of stencil width on surface ocean geostrophic velocity and vorticity estimation from gridded satellite altimeter data. *Journal of Geophysical Research: Oceans*, *117*(C3).
- Ballarotta, M., Metref, S., Albery, A., Cosme, E., Beauchamp, M., & Le Guillou, F. (2021). *Ocean data challenges*. (https://github.com/ocean-data-challenges/2021a_SSH_mapping_OSE)
- Ballarotta, M., Ubelmann, C., Pujol, M.-I., Taburet, G., Fournier, F., Legeais, J.-F., ...

- others (2019). On the resolutions of ocean altimetry maps. *Ocean Science*, *15*(4), 1091–1109.
- Ballarotta, M., Ubelmann, C., Veillard, P., Prandi, P., Etienne, H., Mulet, S., . . . Picot, N. (2023). Improved global sea surface height and current maps from remote sensing and in situ observations. *Earth System Science Data*, *15*(1), 295–315.
- Bretherton, F. P., Davis, R. E., & Fandry, C. (1976). A technique for objective analysis and design of oceanographic experiments applied to mode-73. In *Deep sea research and oceanographic abstracts* (Vol. 23, pp. 559–582).
- Callahan, J. L., Maeda, K., & Brunton, S. L. (2019). Robust flow reconstruction from limited measurements via sparse representation. *Physical Review Fluids*, *4*(10), 103907.
- Cao, Y., Dong, C., Stegner, A., Bethel, B. J., Li, C., Dong, J., . . . Yang, J. (2023). Global sea surface cyclogeostrophic currents derived from satellite altimetry data. *Journal of Geophysical Research: Oceans*, *128*(1), e2022JC019357.
- Chin, T. M., Vazquez-Cuervo, J., & Armstrong, E. M. (2017). A multi-scale high-resolution analysis of global sea surface temperature. *Remote sensing of environment*, *200*, 154–169.
- E.U. Copernicus Marine Service Information (CMEMS). (2024a). *Global ocean along track l3 sea surface heights nrt*. Retrieved from <https://doi.org/10.48670/moi-00147> (Accessed on 07-04-2024)
- E.U. Copernicus Marine Service Information (CMEMS). (2024b). *Global ocean along track l3 sea surface heights reprocessed 1993 ongoing tailored for data assimilation*.

Retrieved from <https://doi.org/10.48670/moi-00146> (Accessed on 07-04-2024)

E.U. Copernicus Marine Service Information (CMEMS). (2024c). *Global ocean-delayed mode in situ observations of surface (drifters, hfr) and sub-surface (vessel-mounted adcps) water velocity*. Retrieved from <https://doi.org/10.17882/86236> (Accessed on 07-04-2024)

Fablet, R., Amar, M. M., Febvre, Q., Beauchamp, M., & Chapron, B. (2021). End-to-end physics-informed representation learning for satellite ocean remote sensing data: Applications to satellite altimetry and sea surface currents. *ISPRS Annals of Photogrammetry, Remote Sensing & Spatial Information Sciences*(3).

Febvre, Q., Sommer, J. L., Ubelmann, C., & Fablet, R. (2023). Training neural mapping schemes for satellite altimetry with simulation data. *arXiv preprint arXiv:2309.14350*.

Gao, Z., Tan, C., Wu, L., & Li, S. Z. (2022, June). Simvp: Simpler yet better video prediction. In *Proceedings of the IEEE/CVF conference on computer vision and pattern recognition (cvpr)* (p. 3170-3180).

Hoskins, B. J. (1982). The mathematical theory of frontogenesis. *Annual review of fluid mechanics*, *14*(1), 131–151.

JPL MUR MEaSURES Project. (2015). *Ghrrsst level 4 mur global foundation sea surface temperature analysis. ver. 4.1*. Retrieved from <https://doi.org/10.5067/GHGMR-4FJ04> (Accessed on 07-04-2024)

Lagerloef, G. S., Mitchum, G. T., Lukas, R. B., & Niiler, P. P. (1999). Tropical pacific near-surface currents estimated from altimeter, wind, and drifter data. *Journal of*

Geophysical Research: Oceans, 104(C10), 23313–23326.

Le Traon, P., Nadal, F., & Ducet, N. (1998). An improved mapping method of multisatellite altimeter data. *Journal of atmospheric and oceanic technology*, 15(2), 522–534.

Manucharyan, G. E., Siegelman, L., & Klein, P. (2021). A deep learning approach to spatiotemporal sea surface height interpolation and estimation of deep currents in geostrophic ocean turbulence. *Journal of Advances in Modeling Earth Systems*, 13(1), e2019MS001965.

Martin, S. A., Manucharyan, G. E., & Klein, P. (2023). Synthesizing sea surface temperature and satellite altimetry observations using deep learning improves the accuracy and resolution of gridded sea surface height anomalies. *Journal of Advances in Modeling Earth Systems*, 15(5), e2022MS003589.

Metref, S., & Ballarotta, M. (2023). *Ocean data challenges*. (https://github.com/ocean-data-challenges/2023a_SSH_mapping_OSE)

Metref, S., Ballarotta, M., Le Sommer, J., Cosme, E., Albert, A., Beauchamp, M., ... Fevre, Q. (2023). *Ocean data challenges*. (<https://ocean-data-challenges.github.io/>)

Okubo, A. (1970). Horizontal dispersion of floatable particles in the vicinity of velocity singularities such as convergences. In *Deep sea research and oceanographic abstracts* (Vol. 17, pp. 445–454).

Penven, P., Halo, I., Pous, S., & Marié, L. (2014). Cyclogeostrophic balance in the mozambique channel. *Journal of Geophysical Research: Oceans*, 119(2), 1054–1067.

- Qiu, B., Chen, S., Klein, P., Sasaki, H., & Sasai, Y. (2014). Seasonal mesoscale and sub-mesoscale eddy variability along the north pacific subtropical countercurrent. *Journal of Physical Oceanography*, *44*(12), 3079–3098.
- Rio, M.-H., Mulet, S., & Picot, N. (2014). Beyond goce for the ocean circulation estimate: Synergetic use of altimetry, gravimetry, and in situ data provides new insight into geostrophic and ekman currents. *Geophysical Research Letters*, *41*(24), 8918–8925.
- Sasaki, H., Klein, P., Qiu, B., & Sasai, Y. (2014). Impact of oceanic-scale interactions on the seasonal modulation of ocean dynamics by the atmosphere. *Nature communications*, *5*(1), 5636.
- Shi, X., Chen, Z., Wang, H., Yeung, D.-Y., Wong, W.-K., & Woo, W.-c. (2015). Convolutional lstm network: A machine learning approach for precipitation nowcasting. *Advances in neural information processing systems*, *28*.
- Srivastava, N., Mansimov, E., & Salakhudinov, R. (2015). Unsupervised learning of video representations using lstms. In *International conference on machine learning* (pp. 843–852).
- Storer, B. A., & Aluie, H. (2023). Flowsieve: A coarse-graining utility for geophysical flows on the sphere. *Journal of Open Source Software*, *8*(84), 4277.
- Storer, B. A., Buzzicotti, M., Khatri, H., Griffies, S. M., & Aluie, H. (2022). Global energy spectrum of the general oceanic circulation. *Nature communications*, *13*(1), 5314.
- Taburet, G., Sanchez-Roman, A., Ballarotta, M., Pujol, M.-I., Legeais, J.-F., Fournier, F., ... Dibarboure, G. (2019). DUACS DT2018: 25 years of reprocessed sea level

- altimetry products. *Ocean Science*, 15(5), 1207–1224.
- Tan, C., Gao, Z., Li, S., & Li, S. Z. (2022). Simvp: Towards simple yet powerful spatiotemporal predictive learning. *arXiv preprint arXiv:2211.12509*.
- Ubelmann, C., Carrere, L., Durand, C., Dibarboure, G., Faugère, Y., Ballarotta, M., . . . Lyard, F. (2022). Simultaneous estimation of ocean mesoscale and coherent internal tide sea surface height signatures from the global altimetry record. *Ocean Science*, 18(2), 469–481.
- Ubelmann, C., Dibarboure, G., Gaultier, L., Ponte, A., Ardhuin, F., Ballarotta, M., & Faugère, Y. (2021). Reconstructing ocean surface current combining altimetry and future spaceborne doppler data. *Journal of Geophysical Research: Oceans*, 126(3), e2020JC016560.
- Vallis, G. K. (2017). *Atmospheric and oceanic fluid dynamics*. Cambridge University Press.
- Weiss, J. (1991). The dynamics of enstrophy transfer in two-dimensional hydrodynamics. *Physica D: Nonlinear Phenomena*, 48(2-3), 273–294.

Region	Mapping Method	RMSE [cm]	RMSE (70-250km) [cm]	Eff. Res. [km]
Gulf Stream (295-305°E, 33-43°N)	DUACS	5.66	2.44	126
	MIOST (geos)	5.61	2.41	120
	NeurOST SSH	5.33	2.29	114
	NeurOST SSH-SST	5.01	2.19	107
	GLORYS	12.47	5.25	236.5
N Atlantic (322-338°E, 39-51°N)	DUACS	4.15	1.33	133
	MIOST (geos + waves)	3.86	1.25	129
	NeurOST SSH	3.85	1.19	121
	NeurOST SSH-SST	3.78	1.12	116
	GLORYS	6.45	2.31	201
Mediterranean (2-19°E, 31-44°N)	DUACS	4.24	1.02	150
	MIOST (geos + waves)	3.97	0.97	128
	NeurOST SSH	3.95	0.98	112
	NeurOST SSH-SST	3.90	0.94	112
	GLORYS	6.25	1.94	220
Kuroshio (153-167°E, 29-41°N)	DUACS	5.03	2.00	163
	MIOST (geos + waves)	4.68	1.80	150
	NeurOST SSH	4.52	1.69	138
	NeurOST SSH-SST	4.34	1.57	128
	GLORYS	8.50	3.14	219
Subtropical N Pacific (149-161°E, 19-31°N)	DUACS	3.79	1.47	197
	MIOST (geos + waves)	3.70	1.39	185
	NeurOST SSH	3.51	1.29	171
	NeurOST SSH-SST	3.42	1.22	156
	GLORYS	5.62	1.89	246
Equatorial Pacific (175-250°E, 10°S-10°N)	DUACS	3.30	1.11	490
	MIOST (geos + waves)	3.21	1.10	445
	NeurOST SSH	3.21	1.10	456
	NeurOST SSH-SST	3.19	1.09	448
	GLORYS	4.17	1.12	499
Brazil-Malvinas (305-325°E, 40-55°S)	DUACS	4.55	1.74	121
	MIOST (geos)	4.45	1.74	118
	NeurOST SSH	4.38	1.67	113
	NeurOST SSH-SST	4.09	1.47	103
	GLORYS	11.28	4.16	248
Agulhas (10-30°E, 35-45°S)	DUACS	6.09	2.55	144
	MIOST (geos + waves)	6.05	2.52	141
	NeurOST SSH	5.78	2.35	127
	NeurOST SSH-SST	5.54	2.19	118
	GLORYS	12.01	4.97	254
Subtropical S Pacific (194-206°E, 19-31°S)	DUACS	3.25	1.11	186
	MIOST (geos + waves)	3.10	1.06	174
	NeurOST SSH	3.05	0.99	162
	NeurOST SSH-SST	2.97	0.93	148
	GLORYS	4.87	1.40	224
Drake Passage (290-300°E, 55-65°S)	DUACS	4.49	1.60	115
	MIOST (geos + waves)	4.44	1.62	110
	NeurOST SSH	4.27	1.53	108
	NeurOST SSH-SST	4.14	1.44	97
	GLORYS	8.68	3.46	230

Table S1: RMSE, filtered RMSE (signals between 70-250km), and effective resolution of the existing global SSH products compared to our deep learning method with and without SST in a selection of regions (Metref & Ballarotta, 2023). We show only the variant of the MIOST method that gives the best RMSE in each region. Bold values indicate the best-performing method on each metric.

Region	Mapping Method	RMSE [cm]	RMSE (70-250km) [cm]	Eff. Res. [km]
Gulf Stream	DUACS	7.50 (5.66)	3.48 (2.44)	159 (126)
	NeurOST SSH-SST	5.58 (5.01)	2.39 (2.19)	115 (107)
N Atlantic	DUACS	4.64 (4.15)	1.64 (1.33)	153 (133)
	NeurOST SSH-SST	3.92 (3.78)	1.23 (1.12)	122 (116)
Mediterranean	DUACS	4.49 (4.24)	1.27 (1.02)	250 (150)
	NeurOST SSH-SST	4.01 (3.90)	1.06 (0.94)	144 (112)
Kuroshio	DUACS	6.16 (5.03)	2.65 (2.00)	197 (163)
	NeurOST SSH-SST	4.65 (4.34)	1.77 (1.57)	139 (128)
Subtropical N Pacific	DUACS	4.21 (3.79)	1.74 (1.47)	227 (197)
	NeurOST SSH-SST	3.54 (3.42)	1.31 (1.22)	169 (156)
Equatorial Pacific	DUACS	3.40 (3.30)	1.14 (1.11)	566 (490)
	NeurOST SSH-SST	3.25 (3.19)	1.10 (1.09)	472 (448)
Brazil-Malvinas	DUACS	5.98 (4.55)	2.55 (1.74)	152 (121)
	NeurOST SSH-SST	4.50 (4.09)	1.74 (1.47)	110 (103)
Agulhas	DUACS	7.85 (6.09)	3.53 (2.55)	176 (144)
	NeurOST SSH-SST	6.05 (5.54)	2.50 (2.19)	128 (118)
Subtropical S Pacific	DUACS	3.51 (3.25)	1.27 (1.11)	206 (186)
	NeurOST SSH-SST	3.03 (2.97)	0.97 (0.93)	155 (148)
Drake Passage	DUACS	4.98 (4.49)	1.96 (1.60)	131 (115)
	NeurOST SSH-SST	4.31 (4.14)	1.56 (1.44)	108 (97)

Table S2: RMSE, filtered RMSE (signals between 70-250km), and effective resolution of the existing global SSH products compared to our deep learning method with and without SST in a selection of regions (Metref & Ballarotta, 2023). We show only the variant of the MIOST method that gives the best RMSE in each region. Bold values indicate the best-performing method on each metric.

Mapping Method	RMSE [cm]	Effective Resolution [km]
DUACS (Taburet et al., 2019)	7.82	152
MIOST (geos) (Ubelmann et al., 2021)	6.93	140
DYMOST (Ubelmann et al., 2015)	6.75	129
BFN-QG (Le Guillou et al., 2021)	7.69	122
4DVarNet SSH (2022) (Beauchamp et al., 2022)	6.63	110
4DVarNet SSH (2023) (Febvre et al., 2023)	6.00	100
MUSTI (Archambault et al., 2023)	6.40	115
ConvLSTM SSH (Martin et al., 2023)	6.46	114
ConvLSTM SSH-SST (Martin et al., 2023)	6.00	100
NeurOST SSH-SST (global)	6.18	114
NeurOST SSH-SST (fine-tuned)	6.04	108

Table S3: RMSE, filtered RMSE (signals between 70-250km), and effective resolution of the existing global SSH products compared to our deep learning method with and without SST in a selection of regions (Metref & Ballarotta, 2023). We show only the variant of the MIOST method that gives the best RMSE in each region. Bold values indicate the best-performing method on each metric.

Region	Mapping Method	RMSE [cm]	RMSE (70-250km) [cm]	Eff. Res. [km]
Gulf Stream	DUACS	7.50 (5.66)	3.48 (2.44)	159 (126)
	NeurOST SSH-SST	5.58 (5.01)	2.39 (2.19)	115 (107)
N Atlantic	DUACS	4.64 (4.15)	1.64 (1.33)	153 (133)
	NeurOST SSH-SST	3.92 (3.78)	1.23 (1.12)	122 (116)
Mediterranean	DUACS	4.49 (4.24)	1.27 (1.02)	250 (150)
	NeurOST SSH-SST	4.01 (3.90)	1.06 (0.94)	144 (112)
Kuroshio	DUACS	6.16 (5.03)	2.65 (2.00)	197 (163)
	NeurOST SSH-SST	4.65 (4.34)	1.77 (1.57)	139 (128)
Subtropical N Pacific	DUACS	4.21 (3.79)	1.74 (1.47)	227 (197)
	NeurOST SSH-SST	3.54 (3.42)	1.31 (1.22)	169 (156)
Equatorial Pacific	DUACS	3.40 (3.30)	1.14 (1.11)	566 (490)
	NeurOST SSH-SST	3.25 (3.19)	1.10 (1.09)	472 (448)
Brazil-Malvinas	DUACS	5.98 (4.55)	2.55 (1.74)	152 (121)
	NeurOST SSH-SST	4.50 (4.09)	1.74 (1.47)	110 (103)
Agulhas	DUACS	7.85 (6.09)	3.53 (2.55)	176 (144)
	NeurOST SSH-SST	6.05 (5.54)	2.50 (2.19)	128 (118)
Subtropical S Pacific	DUACS	3.51 (3.25)	1.27 (1.11)	206 (186)
	NeurOST SSH-SST	3.03 (2.97)	0.97 (0.93)	155 (148)
Drake Passage	DUACS	4.98 (4.49)	1.96 (1.60)	131 (115)
	NeurOST SSH-SST	4.31 (4.14)	1.56 (1.44)	108 (97)

Table S4: RMSE, filtered RMSE (signals between 70-250km), and effective resolution of the existing global SSH products compared to our deep learning method with and without SST in a selection of regions (Metref & Ballarotta, 2023). We show only the variant of the MIOST method that gives the best RMSE in each region. Bold values indicate the best-performing method on each metric.

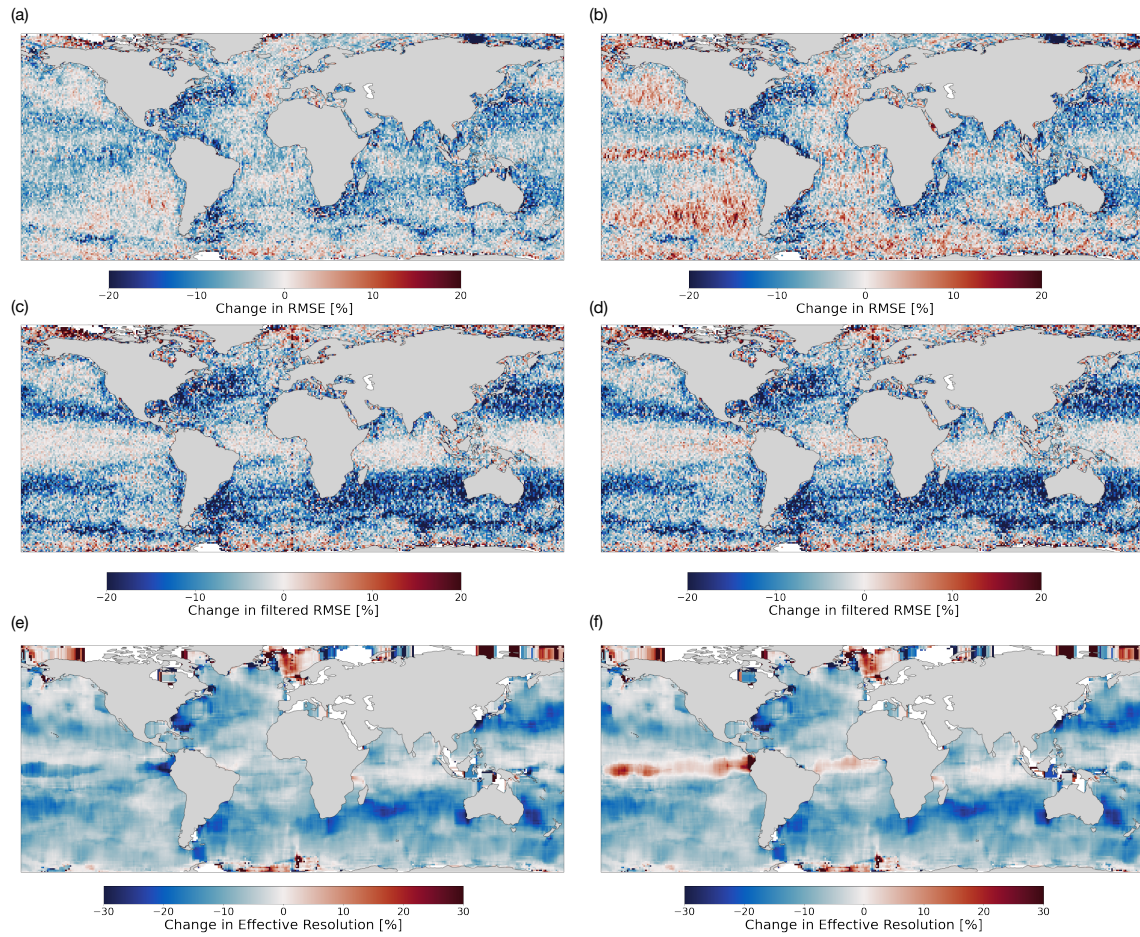


Figure S1: (a) Change in RMSE for NeurOST SSH-SST compared to MIOST (geos.) (b) Same as (a) but for NeurOST SSH-SST compared to MIOST (geos. + waves). (c) Change in RMSE for wavelengths between 70 and 250km for NeurOST SSH-SST compared to MIOST (geos.). (d) Same as (c) but for NeurOST SSH-SST compared to MIOST (geos. + waves). (e) Change in smallest resolved wavelength for NeurOST SSH-SST compared to MIOST (geos.). (f) Same as (e) but for NeurOST SSH-SST compared to MIOST (geos. + waves).

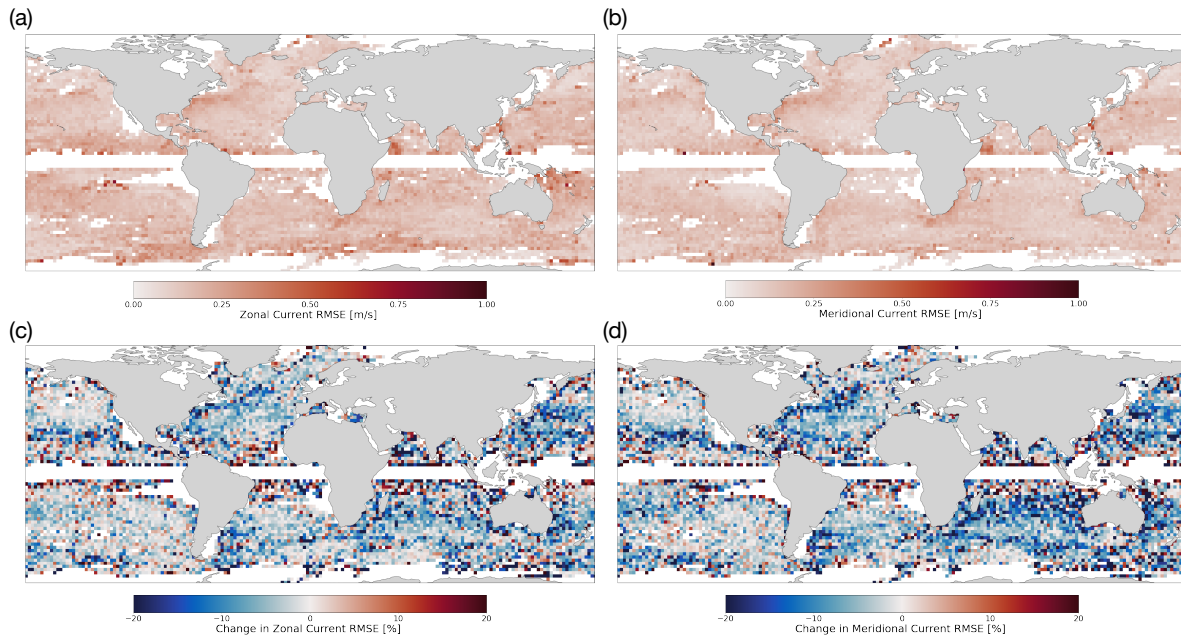


Figure S2: (a) RMSE of NeurOST SSH-SST zonal surface geostrophic currents compared to surface drifters. (b) Same as (a) but for the meridional currents. c, Change in zonal current RMSE for NeurOST SSH-SST compared to DUACS. (d) Same as (c) but for the meridional currents.

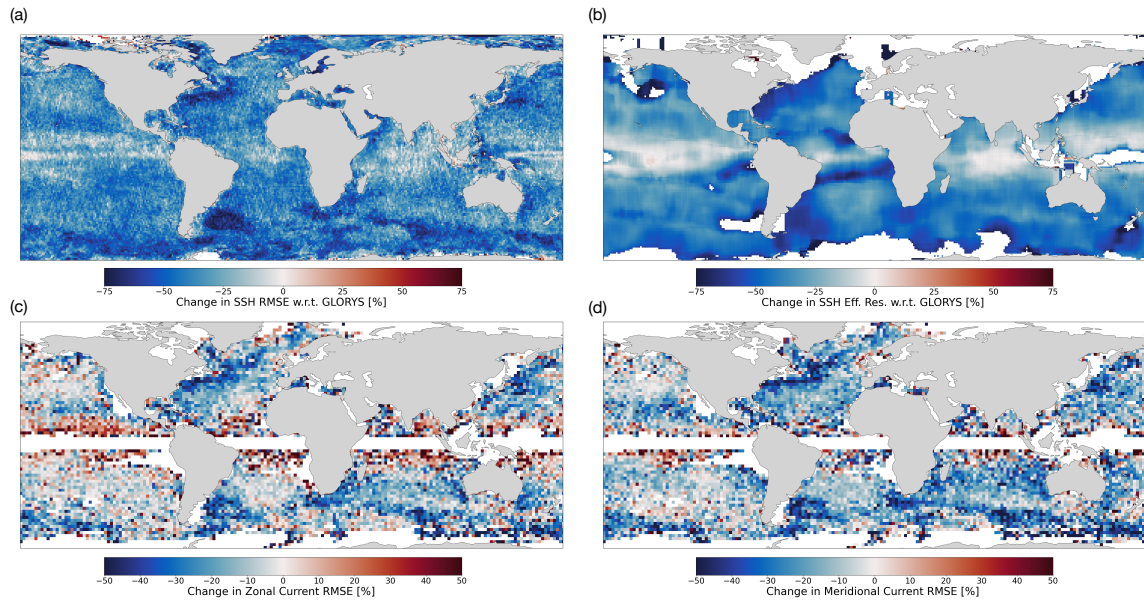


Figure S3: (a) Change in SSH RMSE for NeurOST SSH-SST compared to GLORYS. (b) Same as (a) but for effective spatial resolution. (c) Change in RMSE of zonal surface current for NeurOST SSH-SST compared to GLORYS. (d) Same as (c) but for meridional current.

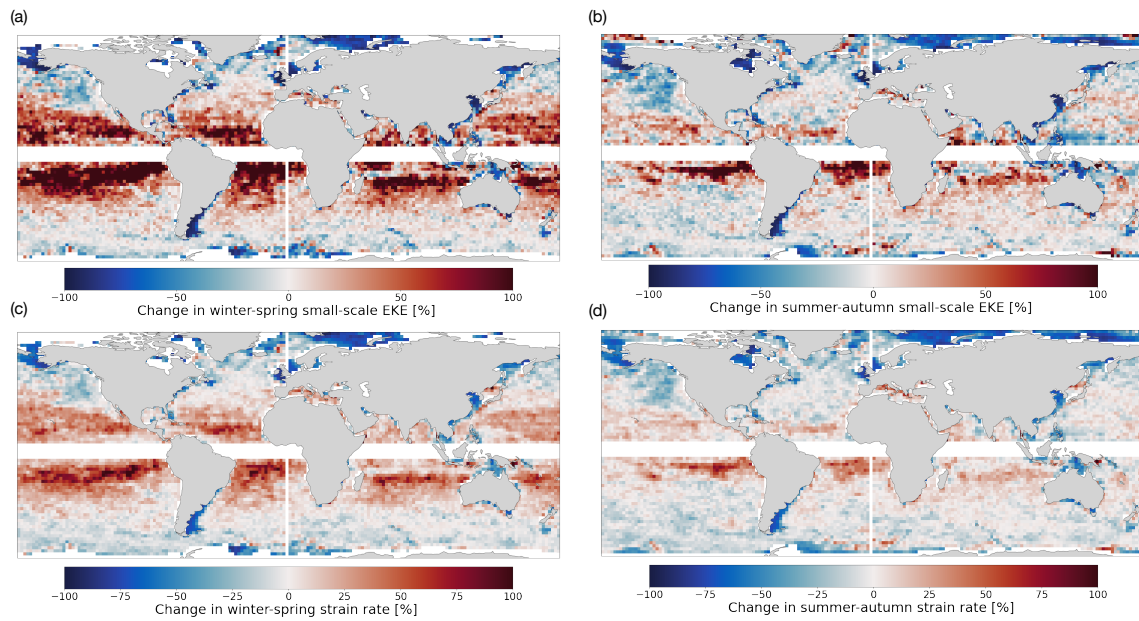


Figure S4: Changes in diagnostics of eddy energy and dynamics from SimVP SSH-SST currents compared to DUACS. (a) Winter-spring mean EKE for flows with wavelength below 250km. (b) Same as (a) but averaged over summer and autumn. (c) Winter-spring mean strain rate. (d) same as (c) but averaged over summer and autumn. Absolute values of these quantities are shown in S.I. Figure S5.

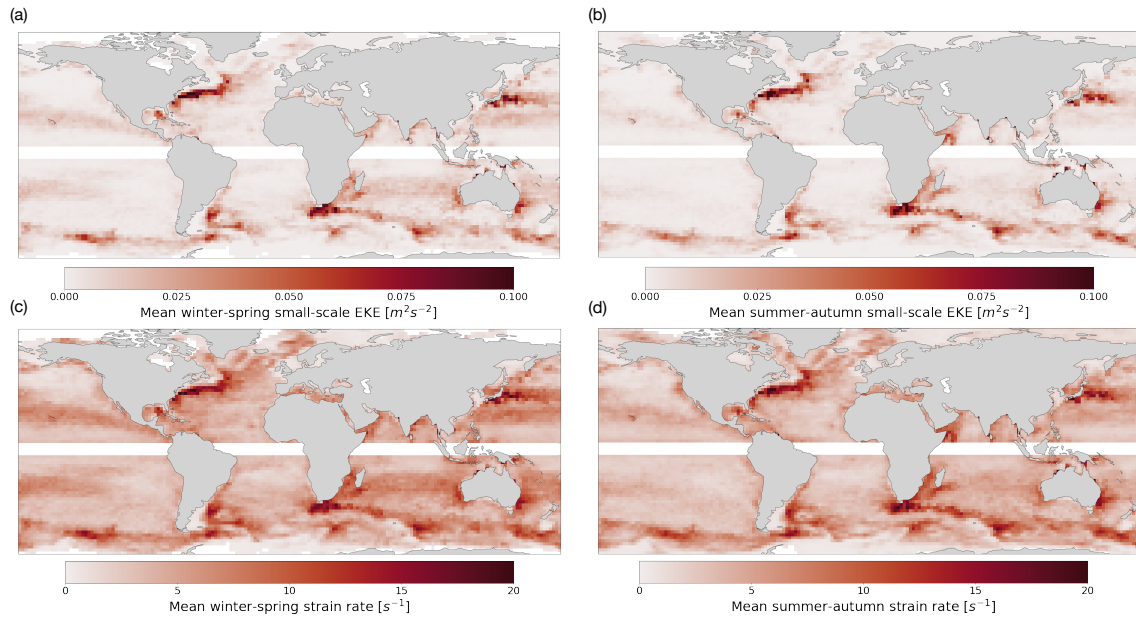


Figure S5: Absolute values of the fields in S.I. Figure S4 calculated from NeurOST SSH-SST maps.

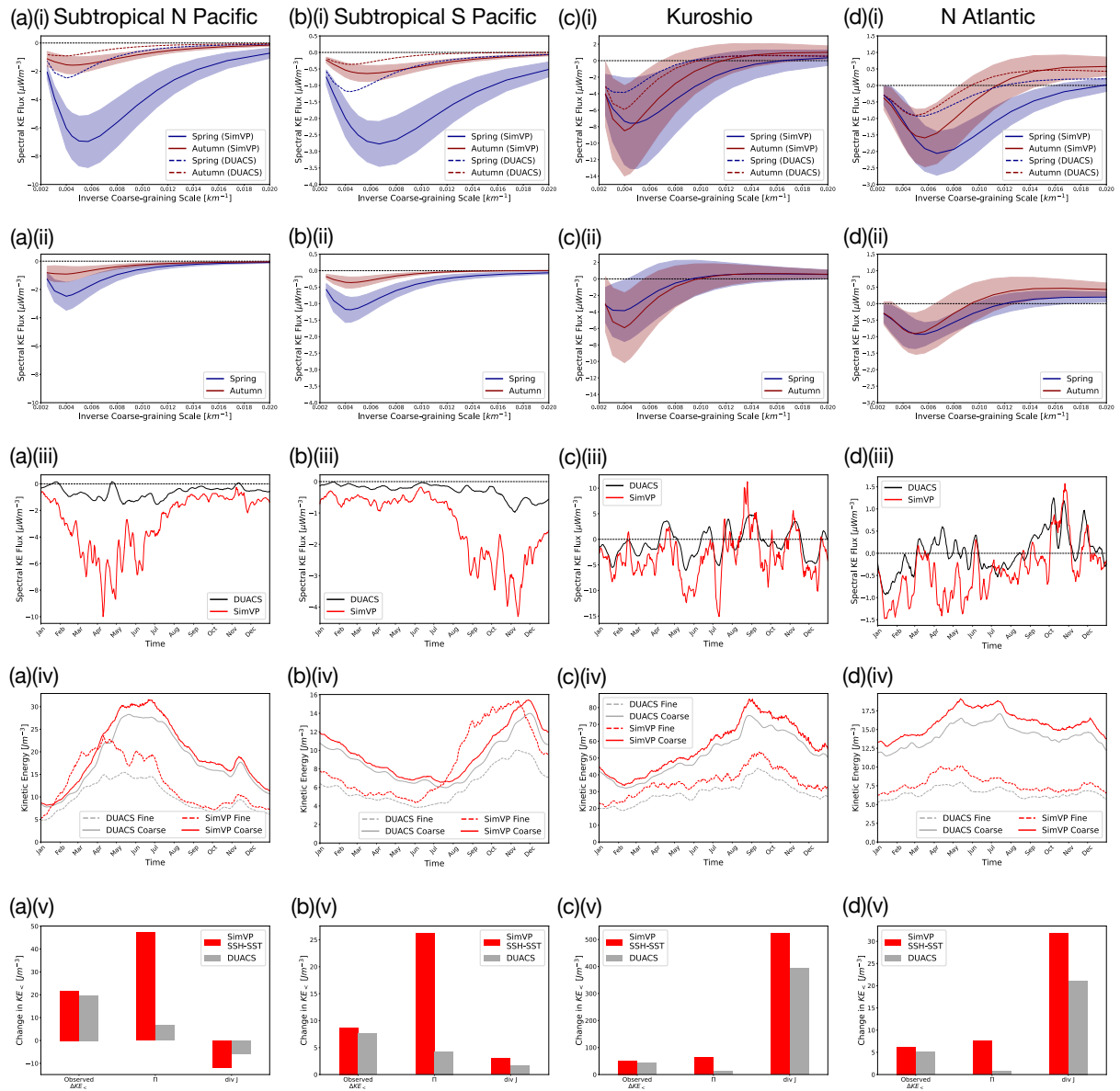


Figure S6: (a) Subtropical North Pacific (149-161E, 19-31N). (i) Mean (solid lines) and standard deviation (shading) of KE cascade from NeurOST SSH-SST surface currents for the seasons of maximum (Spring) and minimum (Autumn) upscale cascade with mean DUACS cascades for reference (dashed lines). (ii) Same as (i) but from DUACS. (iii) Time-series of KE cascade across 250km for both NeurOST SSH-SST and DUACS. (iv) Time-series of coarse- and fine-scale KE (above and below coarse-graining scale of 125km respectively) from both NeurOST SSH-SST and DUACS. (v) Change in KE_{+} (coarse-scale KE) from its wintertime minimum to its summertime maximum compared to the diagnosed contribution from the KE cascade ($-\int \Pi dt$), and the spatial transport of coarse-scale KE ($-\int \nabla \cdot J dt$) for both NeurOST SSH-SST and DUACS. (b)(i-v) Same as (a)(i-v) but for the Subtropical South Pacific (194-206E, 19-31S). (c)(i-v) Same as (a)(i-v) but for the Kuroshio (153-167E, 29-41N). (d)(i-v) Same as (a)(i-v) but for the North Atlantic (322-338E, 39-51N) and with the dividing coarse-graining scale between fine- and coarse-scale KE reduced to 80km.

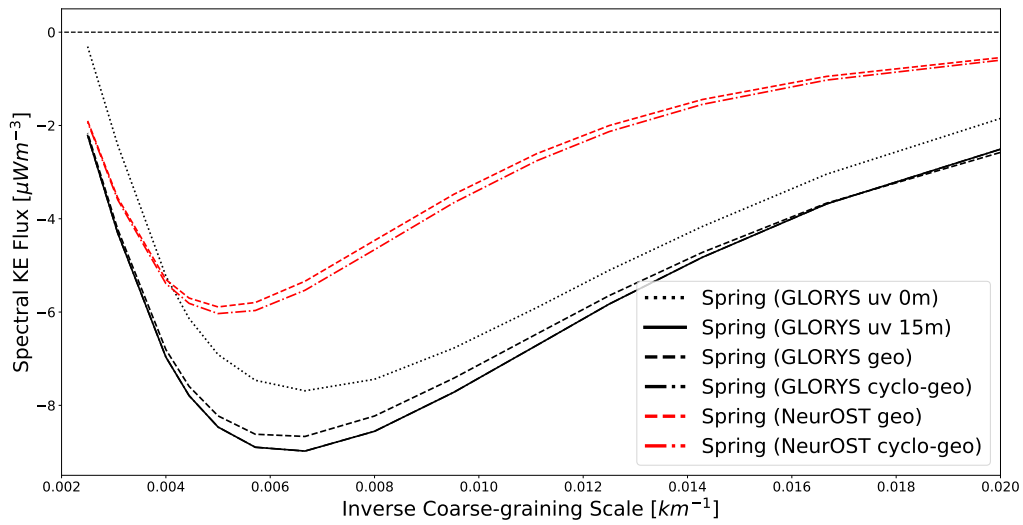


Figure S7: Springtime spectral KE flux estimated from GLORYS and the NeurOST reconstruction of GLORYS from synthetic observations (OSSE) in the Subtropical North Pacific. Results for GLORYS are presented using the total surface currents at 0m and 15m depths ('uv'), using surface geostrophic currents ('geo') calculated from SSH, and using the cyclo-geostrophic correction of Penven et al. (2014) ('cyclo-geo'). Results for NeurOST are presented for both geostrophic and cyclo-geostrophic currents.

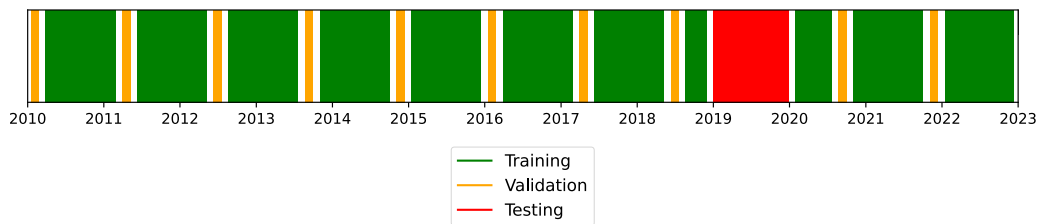
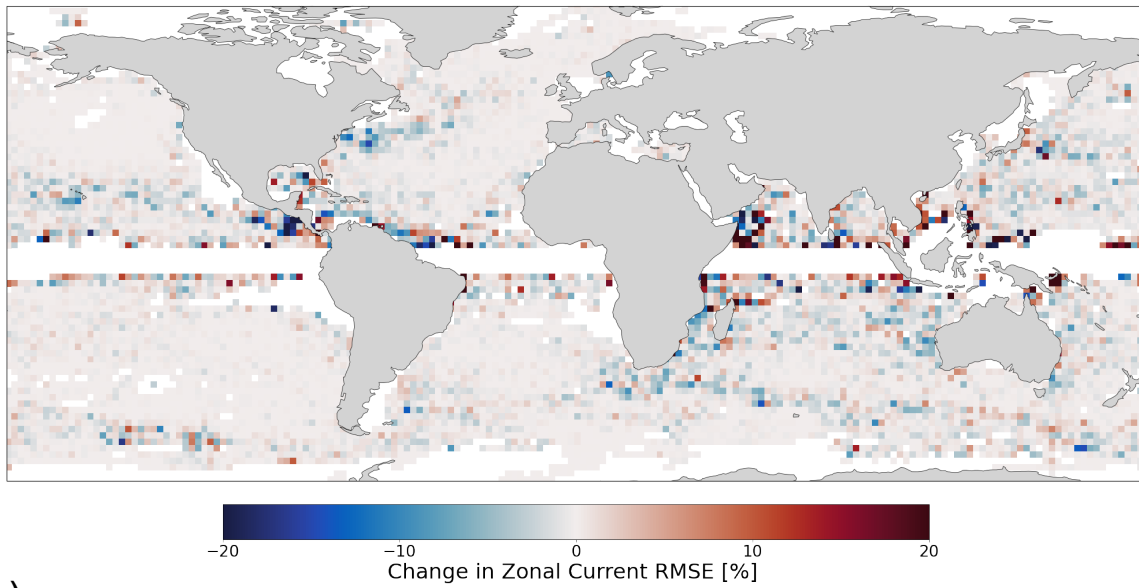


Figure S8: Partitioning of dates between training, cross-validation, and testing when training neural network for SSH mapping.

(a)



(b)

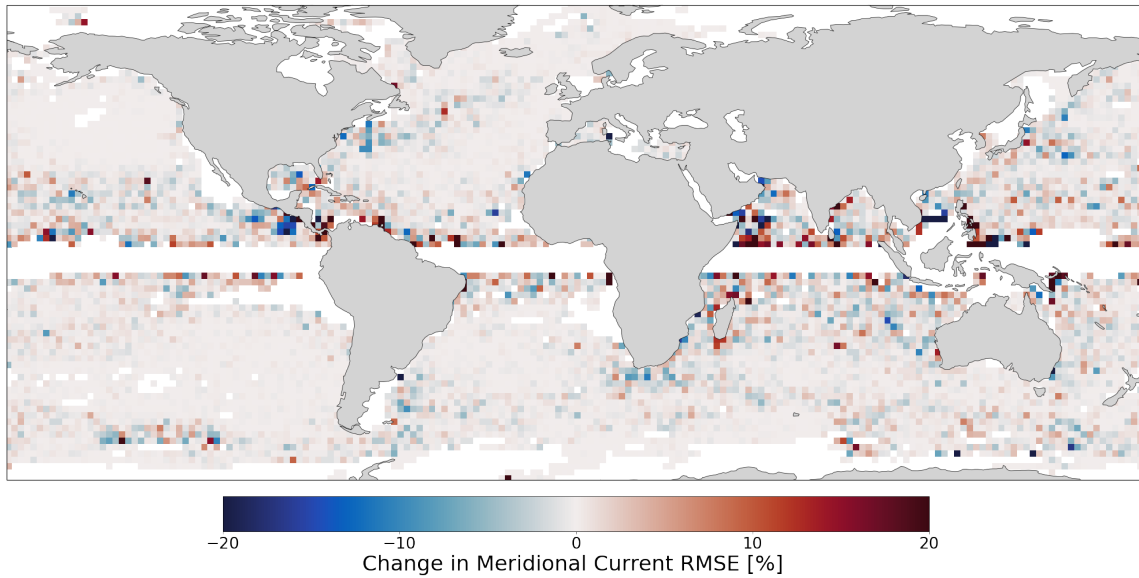


Figure S9: (a) Change in RMSE of zonal current evaluated using drifters when the cyclo-geostrophic correction of Penven et al. (2014) is applied to geostrophic currents from NeurOST SSH-SST. (b) Same as (a) but for meridional currents.